Atmos. Meas. Tech., 16, 1477–1501, 2023
https://doi.org/10.5194/amt-16-1477-2023

Atmospheric Measurement Techniques
Open Access
EGU

Update on the GOSAT TANSO–FTS SWIR Level 2 retrieval algorithm

Yu Someya[1], Yukio Yoshida[1], Hirofumi Ohyama[1], Shohei Nomura[1], Akihide Kamei[1], Isamu Morino[1], Hitoshi Mukai[2], Tsuneo Matsunaga[1], Joshua L. Laughner[3], Voltaire A. Velazco[4,5], Benedikt Herkommer[6], Yao Té[7], Mahesh Kumar Sha[8], Rigel Kivi[9], Minqiang Zhou[10], Young Suk Oh[11], Nicholas M. Deutscher[5], and David W. T. Griffith[5]

[1]Earth System Division, National Institute for Environmental Studies, Tsukuba, Japan
[2]Center for Climate Change Adaptation, National Institute for Environmental Studies, Tsukuba, Japan
[3]Jet Propulsion Laboratory, California Institute of Technology, Pasadena, CA, USA
[4]Deutscher Wetterdienst, Meteorological Observatory Hohenpeissenberg, 82383 Hohenpeissenberg, Germany
[5]Centre for Atmospheric Chemistry, School of Earth, Atmospheric and Life Sciences, University of Wollongong, Wollongong, NSW 2522, Australia
[6]Institute of Meteorology and Climate Research, Karlsruhe Institute of Technology, Karlsruhe, Germany
[7]Laboratoire d'Études du Rayonnement et de la Matière en Astrophysique et Atmosphères (LERMA-IPSL), Sorbonne Université, CNRS, Observatoire de Paris, PSL Université, 75005 Paris, France
[8]Royal Belgian Institute for Space Agency (BIRA-IASB), Brussels, Belgium
[9]Space and Earth Observation Centre, Finnish Meteorological Institute, Tähteläntie 62, 99600 Sodankylä, Finland
[10]CNRC & LAGEO, Institute of Atmospheric Physics, Chinese Academy of Sciences, Beijing, China
[11]National Institute of Meteorological Sciences, 33, Seohbuk-ro, Seogwipo-si, Jeju-do 63568, Republic of Korea

Correspondence: Yu Someya (someya.yu@nies.go.jp)

Received: 11 October 2022 – Discussion started: 8 November 2022
Revised: 3 February 2023 – Accepted: 24 February 2023 – Published: 22 March 2023

Abstract. The National Institute for Environmental Studies has provided the column-averaged dry-air mole fraction of carbon dioxide and methane (XCO_2 and XCH_4) products (L2 products) obtained from the Greenhouse gases Observing SATellite (GOSAT) for more than a decade. Recently, we updated the retrieval algorithm used to produce the new L2 product, V03.00. The main changes from the previous version (V02) of the retrieval algorithm are the treatment of cirrus clouds, the degradation model of the Thermal And Near-infrared Spectrometer for carbon Observation–Fourier Transform Spectrometer (TANSO–FTS), solar irradiance spectra, and gas absorption coefficient tables. The retrieval results from the updated algorithm showed improvements in fitting accuracies in the O_2 A, weak CO_2, and CH_4 bands of TANSO–FTS, although the residuals increase in the strong CO_2 band over the ocean. The direct comparison of the new product obtained from the updated (V03) algorithm with the previous version V02.90/91 and the validations using the Total Carbon Column Observing Network revealed that the V03 algorithm increases the amount of data without diminishing the data qualities of XCO_2 and XCH_4 over land. However, the negative bias of XCO_2 is larger than that of the previous version over the ocean, and bias correction is still necessary. Additionally, the V03 algorithm resolves the underestimation of the XCO_2 growth rate compared with the in situ measurements over the ocean recently found using V02.90/91 and V02.95/96.

1 Introduction

The Greenhouse gases Observing SATellite (GOSAT) is the joint project of the Japan Aerospace Exploration Agency, the Ministry of the Environment, and the National Institute for Environmental Studies (NIES), and it is the first satellite dedicated to monitoring greenhouse gases (GHGs),

such as carbon dioxide (CO_2) and methane (CH_4), from space (Yokota et al., 2009). Since its launch on 23 January 2009, it has constantly provided the global concentrations of GHGs for more than 13 years. Additionally, the successor of GOSAT, GOSAT-2, was launched in 2018 and is also still in orbit. The sensor onboard GOSAT, Thermal And Near-infrared Sensor for carbon Observation (TANSO), consists of two instruments, the Fourier Transform Spectrometer (FTS; Kuze et al., 2009) and the Cloud and Aerosol Imager (CAI). TANSO–FTS measures the spectral regions ranging between 0.758–0.775 µm (12 900–13 200 cm^{-1}), 1.56–1.72 µm (5800–6400 cm^{-1}), and 1.92–2.08 µm (4800–5200 cm^{-1}) in shortwave infrared (SWIR) and 5.56–14.3 µm (700–1800 cm^{-1}) in the thermal infrared (TIR) regions, with a spectral interval of approximately 0.2 cm^{-1} and a spectral resolution (defined as the full width at half maximum of the instrumental line shape function) of 0.262–0.367 cm^{-1} in the SWIR bands (Kuze et al., 2009). The trace gas concentrations or cloud properties have been estimated from the SWIR bands (Yoshida et al., 2011, 2013) and the TIR band (Saitoh et al., 2009, 2016; Ohyama et al., 2012; Someya et al., 2016, 2020).

The SWIR bands measure the reflected sunlight to estimate column-averaged dry-air mole fractions of CO_2 (XCO_2) and CH_4 (XCH_4). NIES provides the SWIR Level 2 (L2) product, which contains XCO_2 and XCH_4 retrieved using the GOSAT SWIR spectra (Yoshida et al., 2011, 2013). The L2 product is used to estimate the global surface fluxes of CO_2 and CH_4 and the resulting concentration distributions provided as Level 4 products (Maksyutov et al., 2013). Other groups have developed retrieval algorithms for GOSAT and provided column-averaged dry-air mole fractions of CO_2 and CH_4 (Butz et al., 2011; Parker et al., 2011; Oshchepkov et al., 2011; O'Dell et al., 2012; Cogan et al., 2012; Kikuchi et al., 2016; Noël et al., 2021; Taylor et al., 2022). The major differences among these algorithms include, e.g., the treatments of atmospheric particles or radiative transfer calculations. The algorithms are roughly classified into two categories considering whether multiple scattering by clouds and aerosols which are critical sources of error is explicitly considered or not.

The current version of the NIES SWIR L2 product is the version 02 series (V02.xx), which has been improved from the previous version in several ways, such as the treatment of the aerosols (Yoshida et al., 2013). Owing to this improvement, both the biases and precisions against the ground-based measurements, the Total Carbon Column Observing Network (TCCON; Wunch et al., 2011), are much less than 1 % for XCO_2 and XCH_4. However, there are still some issues to address. First, the systematic structures in the spectral residuals still exist in the retrieval results. Second, the increase of data amount in the L2 product is further required. In addition, inconsistencies in the annual CO_2 growth rate compared with the in situ measurements were recently found in the V02.90/91 and V02.95/96 products. Therefore, the retrieval algorithm was updated to V03 to address these issues. Herein, we present an algorithm for the new version of the NIES SWIR L2 product, V03.xx.

2 Current retrieval algorithm

2.1 NIES V02 retrieval algorithm

The retrieval algorithm for the SWIR L2 product developed at NIES (Yoshida et al., 2013) is a full physics-based algorithm that explicitly considers the scattering processes by particles in the atmosphere in the radiative transfer calculation. Four spectral ranges, 12 950–13 200 cm^{-1} (O_2 A sub-band), 6180–6380 cm^{-1} (WCO_2 sub-band), 5900–6150 cm^{-1} (CH_4 sub-band), and 4800–4900 cm^{-1} (SCO_2 sub-band), are used for the retrievals. The retrieval algorithm is based on the maximum a posteriori solution (Rodgers, 2000). This method obtains a solution to the state by minimizing the cost function as follows:

$$\mathbf{J}(\boldsymbol{x}) = \left[\boldsymbol{y} - \mathbf{F}(\boldsymbol{x}, \boldsymbol{b})\right]^T \mathbf{S}_\epsilon^{-1} \left[\boldsymbol{y} - \mathbf{F}(\boldsymbol{x}, \boldsymbol{b})\right] + (\boldsymbol{x} - \boldsymbol{x}_\mathrm{a})^T \mathbf{S}_\mathrm{a}^{-1} (\boldsymbol{x} - \boldsymbol{x}_\mathrm{a}),$$

where $\boldsymbol{y}$ represents the measurement vector, $\mathbf{F}$ denotes a forward model, $\boldsymbol{x}$ is a state vector, $\boldsymbol{b}$ denotes a model parameter vector, $\mathbf{S}_\epsilon$ represents a measurement error covariance matrix, $\boldsymbol{x}_\mathrm{a}$ denotes an a priori state vector, and $\mathbf{S}_\mathrm{a}$ represents an a priori covariance matrix. In the NIES retrieval algorithm, the state vector contains the profiles of the gases (CO_2, CH_4, and H_2O) and two types of aerosols, surface albedo over land, wind speed over the ocean surface, surface pressure (P_s), vertically constant temperature shift, zero level offset for the O_2 A sub-band, and wavenumber dispersions for each sub-band. The a priori values of CO_2 and CH_4 are obtained from the NIES transport model (NIES-TM; Saeki et al., 2013) and those of aerosol concentrations are from the Spectral Radiation-Transport Model for Aerosol Species (SPRINTARS; Takemura et al., 2000). Meteorological information is taken from the grid point value (GPV) objective analysis data using the global spectral model (GSM) provided by the Japanese Meteorological Agency. The atmosphere is divided into 15 vertical layers for radiative transfer calculations; the gas optical thickness is calculated every 12 sub-layers in each layer, i.e., 180 sub-layers in total.

2.2 Motivation for algorithm update

Although the number of TANSO–FTS observations in the daytime is approximately 9000 per day, less than 10 % of the total observations pass through the cloud screening and quality control filters to produce the L2 product. Thus, increasing the available number of observations for the L2 product is desirable to increase the TANSO–FTS measurement coverage. The existence of clouds is the main reason for the decrease in the available number of observations. The V02 al-

gorithm discriminates the cloudy scenes using CAI images and the water vapor saturation band near 2 µm, which are mainly used to discriminate optically thick and cirrus clouds, respectively (Yoshida et al., 2011). In the V03 algorithm, cirrus cloud screening using the water vapor saturation band is not applied. Instead, we attempt to retrieve cirrus clouds simultaneously with the GHGs to increase the number of observations.

The spectral residuals obtained from the V02 retrievals have systematic wavenumber-dependent structures. The main causes of these structures are the uncertainties of the solar irradiance spectra and spectroscopic parameters of the trace gases. These datasets are updated to reduce the systematic residuals. In addition, the common use of these datasets with the GOSAT-2 retrievals makes the L2 product from both satellites homogeneous. The homogeneousness of the products makes their continuous and simultaneous use easy.

According to the validation study, biases in the retrieval results of XCO_2 and XCH_4 without bias correction indicate spatial and temporal dependencies, significantly affecting the flux inversions and production of the Level 4 products. Therefore, NIES provides the bias-corrected product (V02.95/96) and the bias-uncorrected one (V02.90/91). Recently, we found that the growth rate of the XCO_2 estimated from the GOSAT L2 product, V02.95/96 or V02.90/91, over the ocean is lower than that over land or the validation data, such as TCCON, and in situ measurements (NIES GOSAT project, 2021). Due to this issue, the GOSAT L2 V02.97/98 product with additional correction applied to its long-term trend based on the bias-corrected V02.95/96 product has been released. The sensitivity degradation of TANSO–FTS could be the main cause of this issue. In this study, the degradation model is updated to decrease the temporal dependencies.

3 Updates on the retrieval algorithm

3.1 Treatment of cirrus clouds

The 2 µm band cloud screening mentioned in Sect. 2.2 is not performed in the V03 algorithm. Alternatively, the spectral band, 5150 to 5200 cm^{-1} (H_2O sub-band), is additionally used in the retrieval to simultaneously estimate the cloud optical thickness (COT) and cloud top pressure (CTP) with GHG concentrations. We assume a single cloud layer with a pressure thickness of 30 hPa in which the ice particles with an effective dimension of 20 µm are homogeneously distributed. The optical property of the ice particle is obtained from the generalized habit mixture model proposed by Baum et al. (2011). The a priori values of COT and CTP are 0.1 and 150 hPa globally. If the retrieved COT is larger than 0.1, the post-screening process rejects the observation.

3.2 Degradation model

The radiometric sensitivity of TANSO–FTS has been degraded exponentially as a function of time relative to the prelaunch calibration with spectral dependencies. The V02 algorithm considers this degradation based on the degradation model developed by Yoshida et al. (2012). The V03 algorithm employs the model recently developed by Someya and Yoshida (2020). This model was constructed from the temporal variations of the principal components obtained from onorbit solar irradiance calibration data using a diffuser plate to distinguish and separately evaluate the components. Although the new degradation model used in V03 and the previous one used in V02 are usually similar, the differences were found with several spectral dependencies. These differences increase with time because the new degradation model was constructed based on the longer data period. Therefore, the update of the degradation model is expected to affect the temporal dependencies of retrieval accuracy. The retrieval results obtained using this model show that the temporal dependency of the XCO_2 bias against the TCCON measurement is reduced with respect to those using the current model in Someya and Yoshida (2020).

3.3 Solar irradiance spectra

The solar irradiance spectra used in the V02 algorithm were created using the baseline estimated from the report by R. Kurucz (http://kurucz.harvard.edu/sun, last access: 13 March 2023) and the Fraunhofer lines personally provided by Geoffrey C. Toon (personal communication, 2011) (Yoshida et al., 2013). The baseline and Fraunhofer lines were updated in V03. The baseline was estimated using the Total and Spectral Solar Irradiance Sensor–1 Hybrid Solar Reference Spectrum (TSIS–1 HSRS; Coddington et al., 2021). Fraunhofer lines were obtained from version 2016 of Toon (2015b).

3.4 Gas absorption coefficient database

In the radiative transfer calculation of retrieval processing, gas absorption coefficients are obtained by interpolating lookup tables (LUTs) as the functions of temperature, pressure, and wavenumber. The LUTs are created using several databases, and the referenced databases were updated (Table 1). Mendonca et al. (2017) found that the CH_4 retrieval using HITRAN 2008 depends on the solar zenith angle. In the V02 retrievals, the residuals at several H_2O absorption lines increase with increasing water vapor because of the large uncertainties in spectroscopic parameters of H_2O. These problems can be resolved or mitigated by the updates. Associated with this update of LUTs, the scaling factor for O_2 absorption (see Sect. 2.3 of Yoshida et al., 2013 for details) is updated to 0.99556. Owing to the updates, the gas absorption coefficient database used in V03 retrievals is com-

Table 1. Summary of the optical parameter updates.

Gas absorption	Reference database	
	V02	V03
O_2	Tran et al. (2006) Tran and Hartmann (2008)	ABSCO V5.0 (Drouin et al., 2017)
CO_2	Lamouroux et al. (2010)	
CH_4	HITRAN 2008 (Rothman et al., 2009)	Devi et al. (2015, 2016) for the $2\nu_3$ band of $^{12}CH_4$ HITRAN 2016 (Gordon et al., 2017) for the others
H_2O	HITRAN 2008	ATM line list 2014 (Toon, 2015a)
H_2O continuum	MT_CKD V2.5.2 (Mlawer et al., 2012)	MT_CKD V3.2

Table 2. Retrieval setup for the V03 product. COT and CTP are additional parameters from V02.

State vector	No. of elements	A priori	Uncertainty
CO_2 mixing ratio	15	NIES-TM	Estimated from NIES-TM
CH_4 mixing ratio	15	NIES-TM	Estimated from NIES-TM
H_2O mixing ratio	15	GPV (GSM)	Estimated from GPV (GSM)
AOT (small particle)	6	SPRINTARS	0.5
AOT (large particle)	6	SPRINTARS	0.5
COT	1	0.1	0.05
CTP	1	150 hPa	30 hPa
Surface pressure	1	GPV (GSM)	5 hPa
Temperature shift	1	0 K	5 K
Surface albedo (over land)	2, 9, 11, 2, 2 (O_2 A, WCO_2, CH_4, H_2O, SCO_2 sub-band)	Estimated from measured spectra	1
Wind speed (over ocean)	1	GPV (GSM)	Estimated from GPV (GSM)
Zero level offset	1 (O_2 A sub-band only)	0 $W\,cm^{-2}\,sr^{-1}/cm^{-1}$	10^{-8} $W\,cm^{-2}\,sr^{-1}/cm^{-1}$
Wavenumber dispersion factor	4 (O_2 A, WCO_2, CH_4, SCO_2 sub-band)	0	10^{-5}

mon to that used in the NIES SWIR L2 retrieval algorithm for TANSO–FTS-2 on GOSAT-2.

3.5 Other changes

In the NIES retrieval algorithm, the empirical noise model was estimated as the quadratic function of the signal-to-noise ratio to define the error covariance matrix (Yoshida et al., 2013). The coefficients of the functions in the V03 algorithm were updated due to the abovementioned changes. The empirical noise is not applied to the H_2O sub-band.

Post-screening is applied to the result after the retrievals, and one of the screening items is the spectral residual. The retrieval results with the mean squared of the residuals normalized with spectral noise larger than the thresholds are screened and not included in the L2 product. The thresholds were re-evaluated as 1.2, 1.2, 1.2, and 1.3 for the O_2 A, WCO_2, CH_4, and SCO_2 sub-bands, respectively. The threshold is undefined for the H_2O sub-band due to its large variability in water vapor concentrations.

Tables 2 and 3 summarize the retrieval setup for the V03 algorithm and the pre-/post-screening procedures for the V02 and V03 algorithms.

4 Results

4.1 Spectral fitting accuracy

Figure 1 shows the averaged spectral residuals after the post-screening at each sub-band obtained in April 2009 and April 2020 over land from V02.90. The plots were normalized with the maximum radiances in each spectral range. These are differences between the simulated radiance spectra using posterior states and the observed spectra. In each sub-band presented in the figure, the residuals exhibit some spectral dependencies. In the O_2 A sub-band, the residuals at the edges of the sub-band are larger than those in the central region, and the structures of the O_2 absorption are seen. In the WCO_2 and CH_4 sub-bands, the residuals have relatively fine structures related to the gas absorptions, although those

Table 3. Summary of the pre-/post-screening procedures for the V02 and V03 algorithm. The observation is rejected if more than one item satisfies the criteria.

Item		Rejection criteria	
		V02	V03
Pre-screening	L1B quality	Bad	
	Out-of-band spectrum	Outlier	
	CAI cloud flag	Cloudy	
	CAI coherent (ocean)	Cloudy	
	2 µm band cloud flag	Cloudy	–
	Solar zenith angle	$> 70^{\circ}$	
	SNR	< 70 for O_2 A sub-band	
	Land fraction	$0\,\% <$ and $< 60\,\%$	
Post-screening	No. of iterations	20	
	Mean squared residuals (O_2 A, WCO_2, CH_4, and SCO_2 sub-bands)	> 1.2, 1.2, 1.3, and 1.4	> 1.2, 1.2, 1.2, and 1.3
	Degree of freedom for signal	< 1	
	AOT (1.6 µm)	> 0.1	
	Blended albedo	> 1	
	Surface wind speed	< 0.1 or $> 20\,\mathrm{m\,s^{-1}}$	
	Absolute difference between retrieved and a priori P_s	$> 20\,\mathrm{hPa}$	
	COT	–	> 0.1

Table 4. Root mean squares of the averaged spectral residuals for each sub-band in April 2020. The unit is $\times 10^{-9}\,\mathrm{W\,cm^{-2}\,sr^{-1}\,cm^{1}}$.

		O_2 A	WCO_2	CH_4	SCO_2
V02.90/91	Land	1.429	0.973	0.811	0.834
	Ocean	1.219	0.859	0.980	0.762
V03.00	Land	1.217	0.854	0.612	0.799
	Ocean	1.161	0.687	0.613	1.206

at the edges and in the center are flattened. Figure 2 shows the spectral residuals as the same as in Fig. 1, except that V03.00 is used. Compared with Fig. 1, the wavenumber dependencies of the residuals are decreased, and the retrievals seem to be well fitted in Fig. 2. The same figures over the ocean are shown in Figs. 3 and 4. The same as over land, the fitting accuracies of V03.00 are found to be better than those of V02.90 in the O_2 A, WCO_2, and CH_4 sub-bands. However, in the SCO_2 sub-band, the residual has a significant spectral dependency, and it corresponds to the CO_2 absorption structure. The root mean squares of the averaged spectral residuals in April 2020 shown in the figures are summarized in Table 4. The values from V03.00 are lower than the values from V02.90/91, and the spectral fitting accuracies are improved except for the SCO_2 sub-band over the ocean.

The abovementioned differences in spectral residuals between V02.90 and V03.00 are mainly due to the update of the solar irradiance and gas absorption cross-section database. This is because the treatment of clouds has a smaller impact on the fine structure of the residuals, and there are slight spectral dependencies of differences between the new and old degradation models shortly after the launch. The update of solar irradiance decreased the relatively large wavenumber dependencies, such as the large residuals around $6375\,\mathrm{cm^{-1}}$ and the large wavenumber dependency around $6000\,\mathrm{cm^{-1}}$ shown in Fig. 3. Updating the gas absorption cross-section database significantly improves the fitting accuracy in the CH_4 sub-band and substantially decreases the fine structure of the residuals. The O_2 A sub-band is flattened, and the differences between the center and edges of the sub-band are decreased by both the updates of solar irradiance and gas absorption coefficients. However, in the O_2 A sub-band, some differences between 2009 and 2020 remain. One possible reason for this is the degradation model. The number of components of principal component analysis used to construct the degradation model in the O_2 A sub-band is smaller than the other band because the contributions of the primary components are large. The temporal differences are possibly due to the contributions from the other components, which are not considered in the construction of the degradation model.

Figure 4 shows the significant spectral dependencies of the residuals obtained from V03.00 in the SCO_2 sub-band over the ocean. In this figure, the baselines of the simulated radiance spectra seem to have some biases. This is introduced by the update of the solar irradiance spectra, because there are some differences in the spectral baseline between the old and updated spectra particularly in band 3 (see Appendix A and Supplement). Over the ocean, the surface state is described only by the surface wind speed in the retrieval, and the spec-

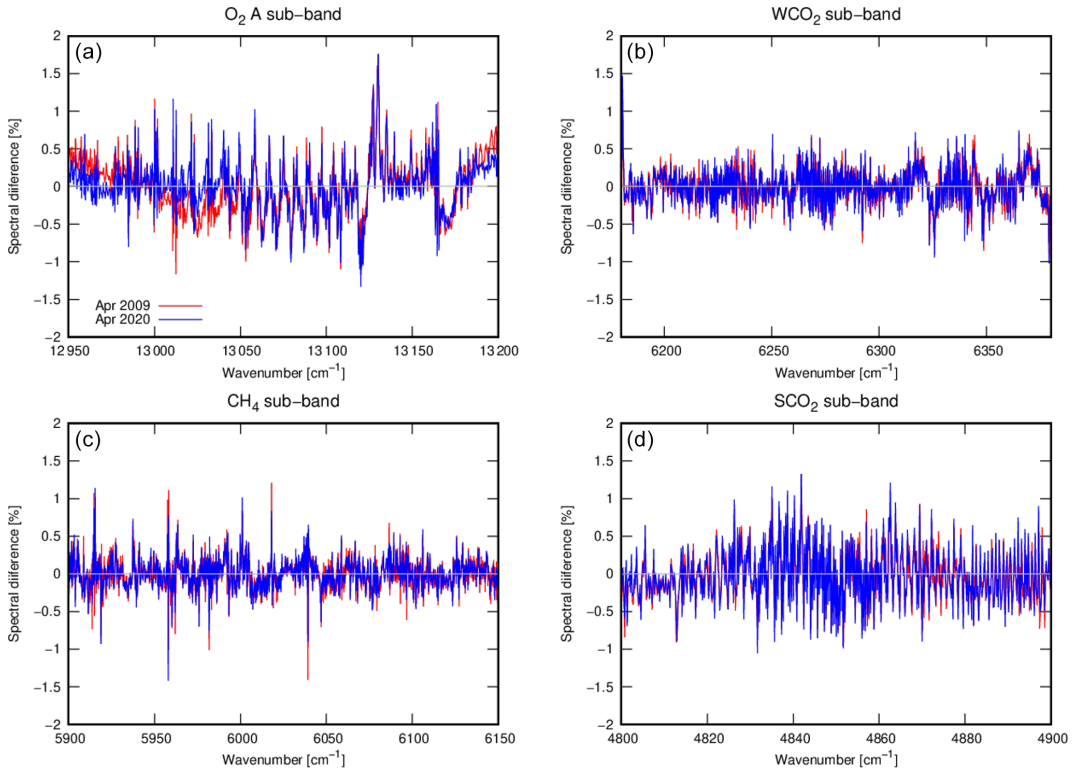

Figure 1. Averaged spectral residuals (simulated minus observed) normalized with the maximum radiance in each range at O_2 A **(a)**, WCO_2 **(b)**, CH_4 **(c)**, and SCO_2 **(d)** sub-bands in April 2009 (red) and April 2020 (blue) over land obtained from V02.90.

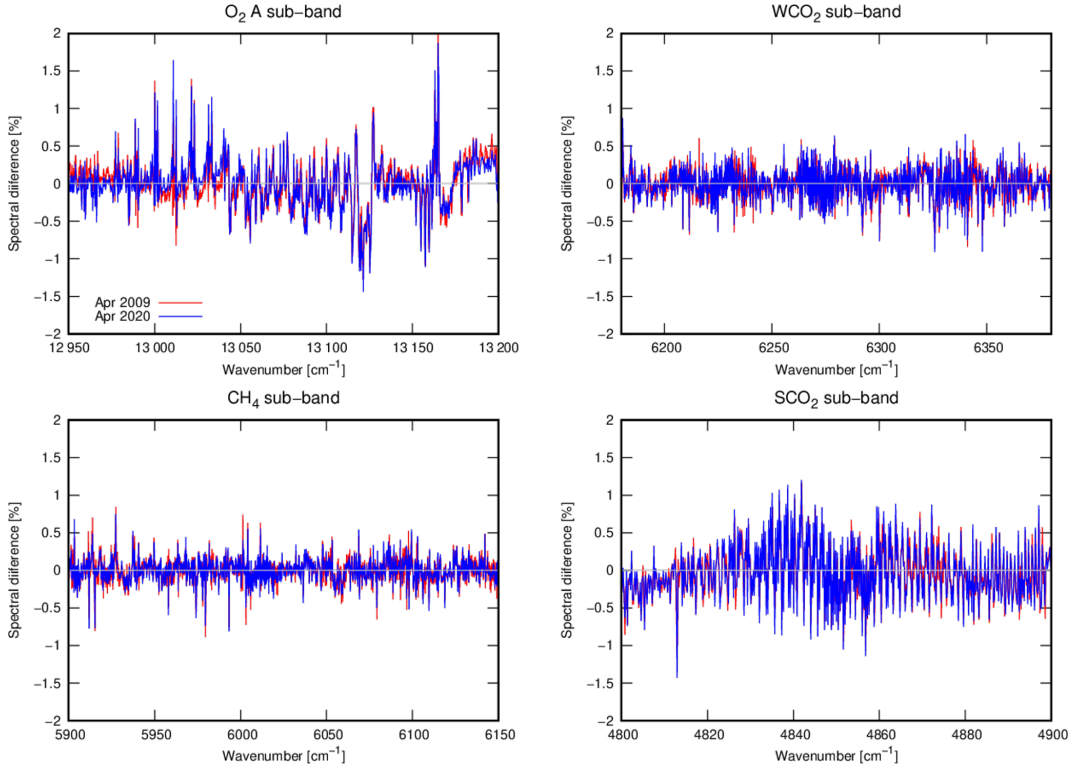

Figure 2. Same as Fig. 1, but for V03.00.

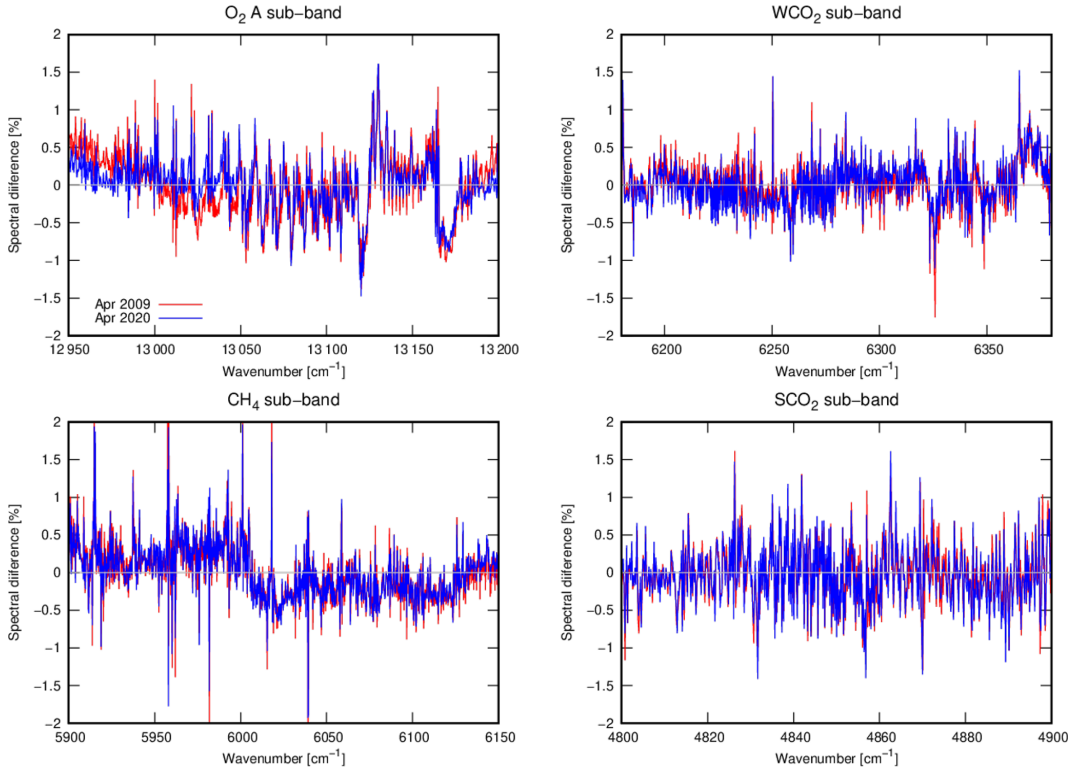

Figure 3. Same as Fig. 1, but for over the ocean.

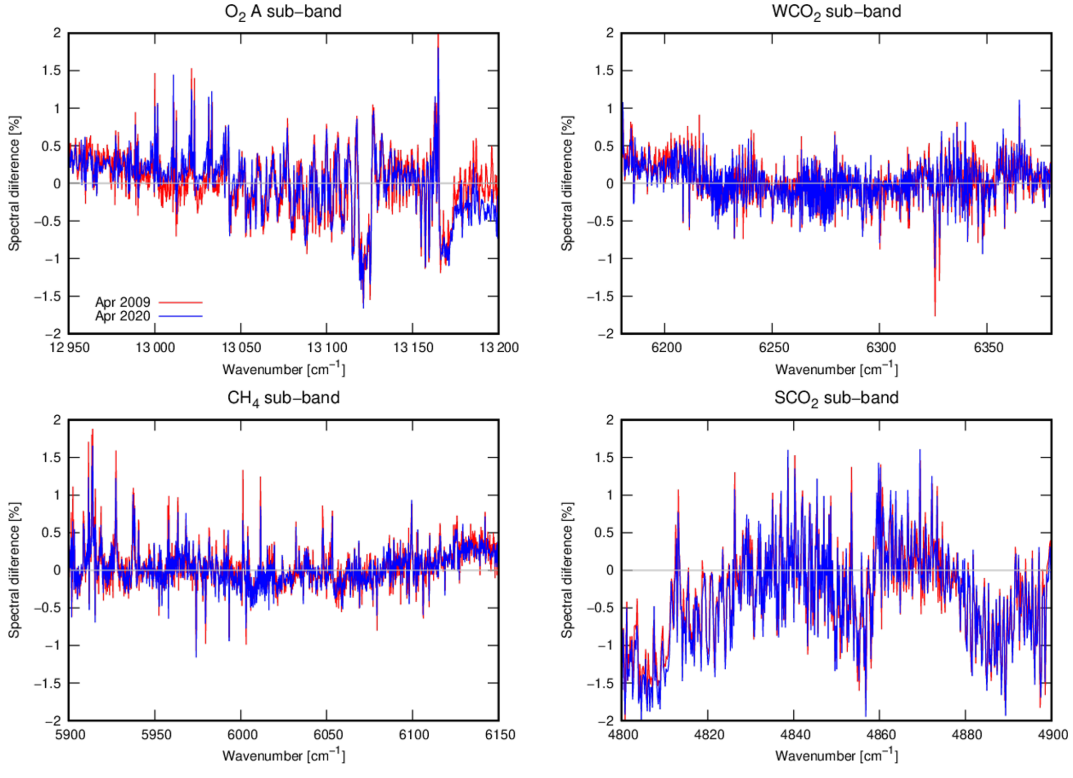

Figure 4. Same as Fig. 3, but for V03.00.

tral baseline is not adjusted (unlike that for over land). The spectral structure corresponding to CO_2 absorption is found in this figure. This can be the result of changes in retrieved CO_2 to reduce residuals due to baseline bias. This can lead to a bias in the retrieved XCO_2. Therefore, we need to precisely evaluate the calibration data, such as those obtained in the Railroad Valley campaign, using the updated solar irradiance spectra to improve the fitting accuracy especially on the SCO_2 sub-band.

4.2 Global distribution of the retrieval results

In this section, we show the difference in the retrieval results between V02.90/91 and V03.00. The data from the launch until 2021 are used for both versions. Global distributions of the retrieved XCO_2 (for V02.90/91, V03.00, and their differences), XCH_4 (for V02.90/91, V03.00, and their differences) and the number of observations (for V02.90/91, V03.00, and their differences) are shown in Figs. 5 and 6 separately over land and the ocean. The XCO_2 from V03.00 over land is approximately the same as that from V02.90/91. Conversely, over the ocean, the XCO_2 from V03.00 is 4.24 ppm lower than that from V02.90/91 for the match-up observations. This difference arises due to the spectral residual in the SCO_2 sub-band mentioned in Sect. 4.1.

The XCH_4 from V03.00 is lower than that from V02.90/91 globally. The changes in XCH_4 are commonly shown with a magnitude of approximately 8 ppb over land and the ocean. It is largely decreased in the middle and low latitudinal areas. Although it is difficult to isolate the impacts of each update on the retrieval results, our sensitivity test revealed that the XCH_4 over land changed by approximately 7 ppb depending on whether solar irradiance spectra are updated or not. On the other hand, the other test with the replacement of the gas absorption table shows smaller changes in XCH_4 over land (See Appendix A). These may indicate that the decrease in XCH_4 is mainly because of the update of the solar irradiance spectra.

The temporal heat maps of the differences in the monthly mean XCO_2 and XCH_4 between the versions are shown in Fig. 7. The differences in monthly mean XCO_2 get smaller with time, particularly over the ocean. This means that the growth rate of XCO_2 from V03.00 is larger than that from V02.90/91. The long-term trend in XCO_2 is evaluated using the in situ measurements in Sect. 4.4. Similar trends are also seen in XCH_4. Additionally, the seasonal variabilities of XCH_4 are larger than those of XCO_2, especially for the former period over the ocean. This is partly because the changes in XCH_4 over the ocean have latitudinal dependencies, as shown in Fig. 6. The global distributions of the seasonal mean XCO_2 and XCH_4 in 2010 and 2021 are shown in Fig. 8. As seen in Figs. 5–7, the differences are smaller in the recent period, and they have latitudinal dependencies. In addition, the latitudinal variations change seasonally, as shown in Fig. 8. The increasing trend of XCO_2 in the high latitudes in Fig. 5 is introduced by the change in boreal spring (MAM), and this is not seen in boreal summer (JJA). A similar characteristic is also seen in XCH_4.

Table 5. Number of observations from the V02.90/91 and V03.00 XCO_2 products and their differences for each surface type from the launch to 2021.

	V02.90/91	V03.00	Difference (%)
Land	960 394	1 082 768	+12.7 %
Ocean	557 488	444 477	−20.3 %
Mixed	130 836	159 960	+22.3 %
Total	1 648 718	1 687 205	+2.3 %

The number of observations over land is increased significantly because the 2 µm cloud screening is not applied in V03 retrievals. Because the XCO_2 values over land from V02.90/91 and V03.00 have only slight differences, the addition of the cirrus cloud parameters is effective in increasing the number of observations. However, the number of observations over the ocean is decreased, except in the intertropical convergence zone where cirrus clouds frequently exist because the residuals in the SCO_2 sub-band are increased, and more observations are filtered through the post-screening process in the V03.00 retrieval. The numbers of observations from the V02.90/91 and V03.00 XCO_2 products are shown in Table 5. The V03.00 product increases the number of observations obtained over land and the mixed surface of land and ocean, by 12.7 % and 22.3 %, compared with the V02.90/91 product, respectively.On the other hand, it decreases by 20.3 % over the ocean. Overall, the number of available observations from V03.00 is 2.3% larger than that from V02.90/91.

Figure 9 shows the global distributions of the ancillary parameters, the difference between the retrieved and a priori surface pressures (ΔP_s), retrieved temperature shift, large-particle AOT, and the COT from V02.90/91 and V03.00. These results are obtained only from the observations that passed the post-screening process; those with large AOT and COT (> 0.1) are excluded. The general ΔP_s patterns are similar for V02.90/91 and V03.00. Over land, negative biases are slightly improved in V03.00. Over the ocean, positive biases are large in the high latitudes of the Southern Hemisphere for V02.90/91 and low latitudes for V03.00. The horizontal pattern of ΔP_s over land in the middle and low latitudes seems to correspond to that of the difference in XCH_4 shown in Fig. 5. Correlation coefficients between the changes in the retrieved surface pressure and those in XCH_4 from V02.90/91 and V03.00 are -0.57 over land and -0.64 over the ocean. The relatively large decrease in XCH_4 in low latitudes over the ocean could be partly attributed to the changes in ΔP_s. For XCO_2, those are -0.57 over land and -0.11 over the ocean. Negative biases of the temperature shift decreased globally for V03.00 and those over the ocean for

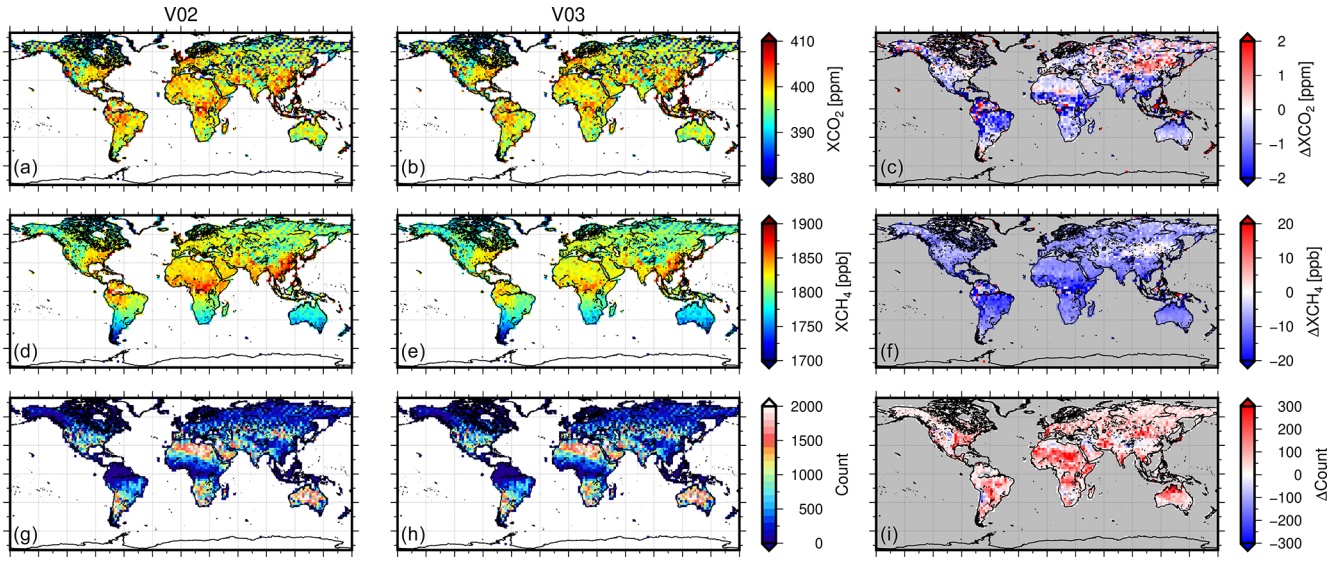

Figure 5. Global distributions of XCO_2 **(a–c)**, XCH_4 **(d–f)**, and the number of observations **(g–i)** for V02.90/91 **(a, d, g)**, V03.00 **(b, e, h)**, and their differences **(c, f, i)** from the launch to 2021 over land and mixed surface. The values are averaged or integrated within 2.5° × 2.5° grid boxes. All the observations were used for each version.

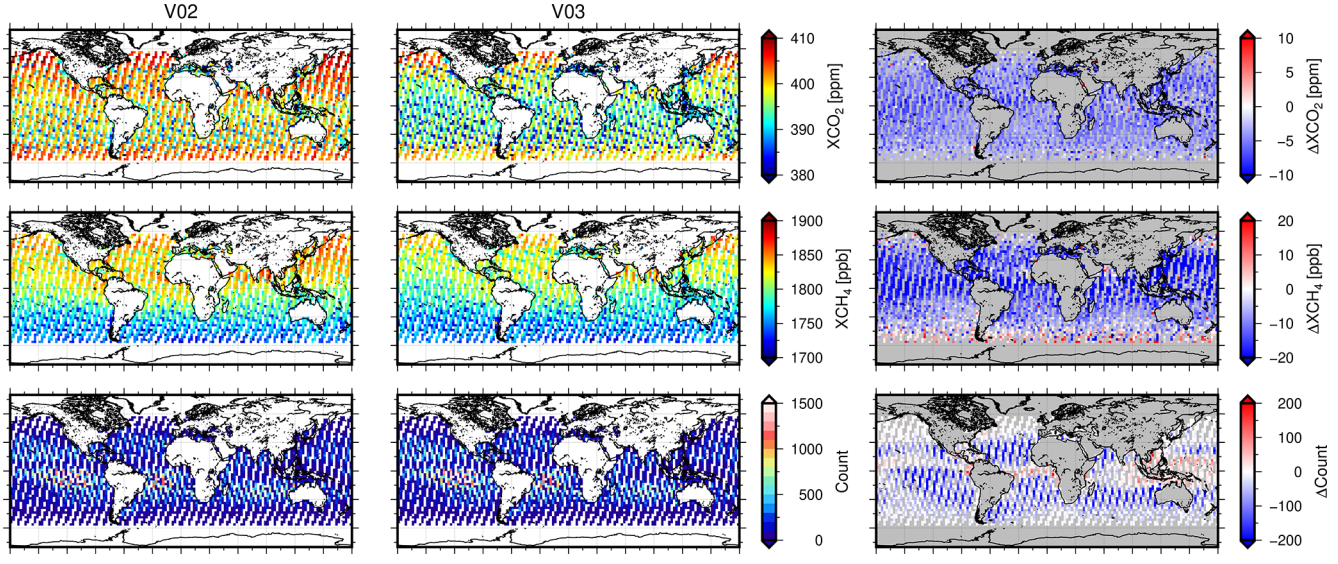

Figure 6. Same as Fig. 5, but for over the ocean.

V02.90/91 changed to slightly positive biases. Although the relatively large negative biases remain in inland China for V03.00, those in Europe and America for V02.90/91 become smaller for V03.00. The AOT of large particles at 1.6 µm decreased globally, especially over the ocean for V03.00. The COT is obtainable only for V03.00. Although the observations with large COT values are rejected by post-screening, the relatively large values are seen in the tropical regions, where cirrus clouds are frequently present.

Although the updated items do not independently affect the retrieval results and it is difficult to evaluate separately, the large causes of the change in the retrieved ancillary parameters are as follows from the sensitivity test retrievals (Appendix A). The temperature shift is increased globally by the update of the gas absorption coefficient tables. Surface pressure seems to be impacted by the replacement of solar irradiance because ΔP_s was changed by this update over land. The changes in surface pressure should contain two effects. One is the direct impact of the change in spectroscopy on the O_2 A sub-band. The other one is the impact through the change of XCO_2 introduced by the inconsistency of the spectral baseline in the SCO_2 sub-band. The behaviors of changes

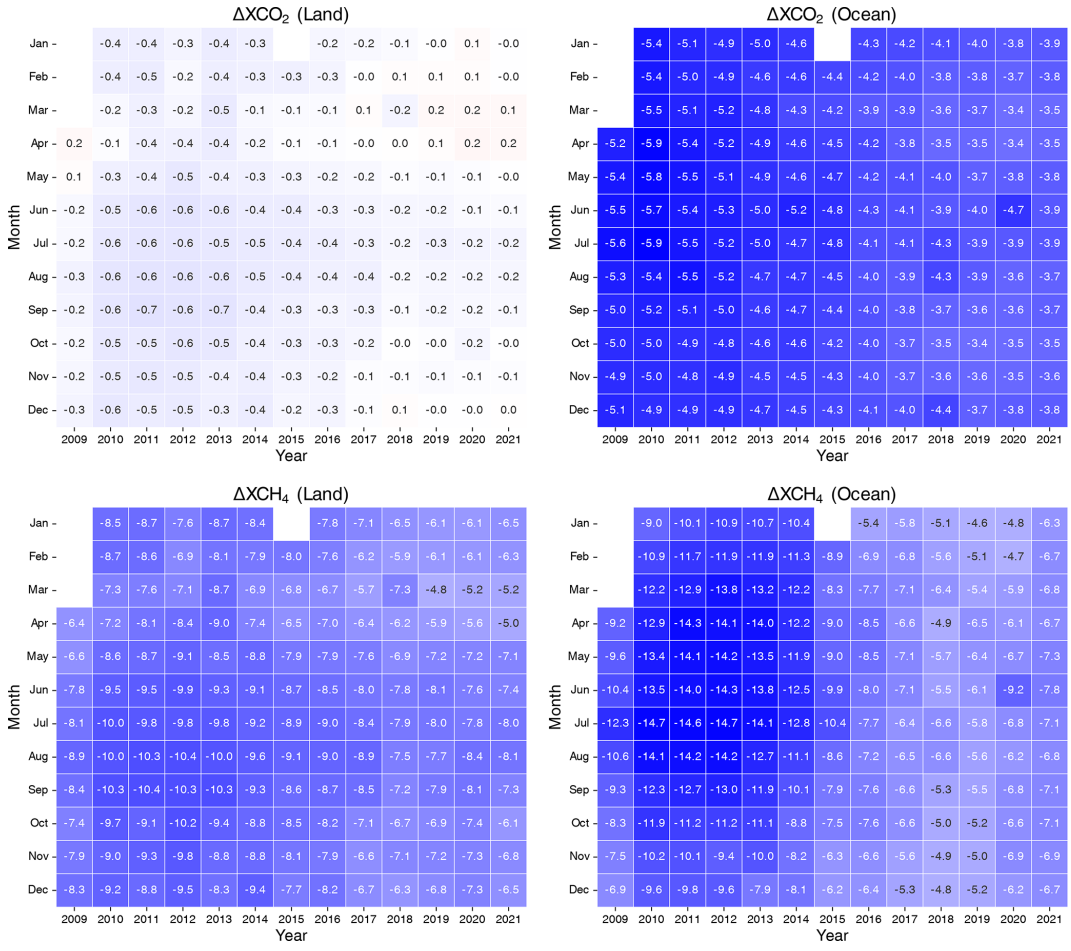

Figure 7. Time series heat maps of the differences in monthly mean XCO_2 and XCH_4 over land and the ocean between V02.90/91 and V03.00 (V03.00 minus V02.90/91). Only the observations commonly available for both versions were used. The units for XCO_2 and XCH_4 are ppm and ppb.

in AOT differ for land and the ocean. The changes in AOT are mainly affected by the addition of cirrus properties to the state vector over land. On the other hand, those over the ocean seem to be affected multiply by the updates. Figure 10 shows the time series of the ancillary parameters. V02.90/91 has a long-term temporal dependency on the retrieved surface pressure over land, temperature shift, and AOT over the ocean. The pointing system of TANSO–FTS was switched from the primary system (PM–A) to the backup system (PM–B) on 26 January 2015. The trends differ for PM–A or PM–B, and they are larger in PM–A. For V03.00, those in surface pressure and AOT almost disappeared, whereas those in the temperature shift remain in PM–A.

4.3 Comparison with TCCON measurements

The retrieved XCO_2 and XCH_4 are validated using the TCCON measurements in this section. The TCCON sites used in this study are listed in Table B1. The GOSAT measurements used for the comparisons are selected within $\pm 2^\circ$ from each TCCON site. The TCCON measurements within ± 30 min from the GOSAT measurement time are averaged for comparison. We used the data from the launch to 2021. Currently, the newest TCCON product, version GGG2020, is provided, and we used this version in this analysis. However, not all sites have produced their full GGG2020 time series at the time of writing. The main changes between GGG2020 and the previous version, GGG2014, are found on the TCCON wiki page (https://tccon-wiki.caltech.edu/Main/DataDescriptionGGG2020, last access: 13 March 2023). The data amount of GGG2020 is currently smaller than that of GGG2014 because of stricter quality control processes, but much of these data should be recovered in the near future. In particular, measurements collected before 2011 are sparse.

The comparison results for V03.00 and V02.90/91 versus TCCON are shown in Table 6. Bias means the average of the differences between GOSAT and TCCON, and the standard deviations are calculated from these differences. The GOSAT measurements are categorized according to the surface state and the gain (high: H or middle: M) setting of

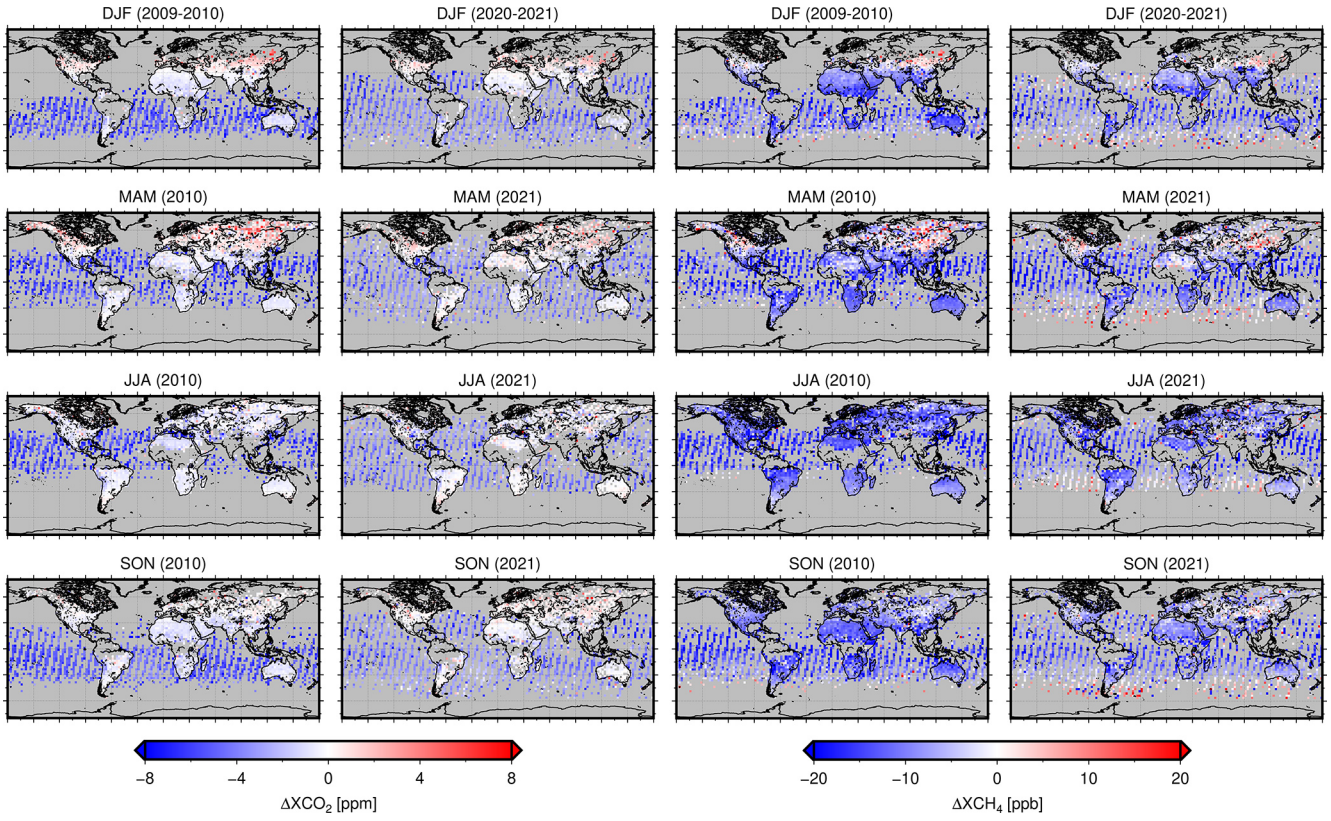

Figure 8. Global distributions of the differences in seasonal mean XCO_2 (left eight panels) and XCH_4 (right eight panels) in 2010 and 2021. The grid size is the same as Fig. 5. All the observations were used for each version.

the FTS measurement. The observations containing both the land and ocean surfaces in the instantaneous field of views of TANSO–FTS are not used here. The number of observations with gain H from V03.00 is larger than that from V02.90/91 over land. On the other hand, those with gain M from V03.00 are slightly smaller than those from V02.90/91. The sites used for gain M are only two sites, Pasadena and Jet Propulsion Laboratory (JPL), which are very close to each other and located near Los Angeles. Over the ocean, the number of observations from V03.00 decreases. There are no substantial changes in the standard deviations of the differences for XCO_2 and XCH_4 in all the situations (slightly worse in V03.00), although the biases are different between V03.00 and V02.90/91 in some cases.

The biases and standard deviations of the XCO_2 from V03.00 are close to those from V02.90/91 over land. Considering these results, the XCO_2 from V03.00 has similar qualities as that from V02.90/91 over land. Meanwhile, the bias of the XCO_2 from V3.00 is larger and more negative than that from V02.90/91 over the ocean. This issue is consistent with the results presented in Sect. 4.2 and is because of the fitting accuracy shown in Sect. 4.1. Therefore, the bias correction seems necessary for the XCO_2 from V03.00 over the ocean.

As shown in Sect. 4.2, the XCH_4 from V03.00 decreased from those from V02.90/91. Over land, the absolute values of the XCH_4 from V03.00 are slightly larger with gain H and significantly smaller with gain M than those from V02.90/91. Over the ocean, the bias from V03.00 is larger, although a smaller data amount is available. Therefore, we need to investigate the biases over the ocean with a larger amount of data in the future.

The validation results over land with gain H in the stricter match-up condition of $\pm 0.1°$ are shown in Table 7 to investigate these differences more precisely. Because of the spatial variability of GHGs, the validation with the stricter condition is more reliable, especially for XCH_4. Unfortunately, there are no match-up data found over land with gain M and over the ocean in this match-up condition. In this table, the absolute values of bias and standard deviation of the XCH_4 from V03.00 are smaller than those from V02.90/91. Therefore, the quality of the XCH_4 from V03.00 can be regarded as almost the same as or better than those from V02.90/91. Similar to the results from the looser match-up condition, the results of XCO_2 from V03.00 increase the number of observations and are slightly worse biases and standard deviations.

Intersite and temporal variability of the differences between GOSAT and TCCON are investigated using the match-up condition of $\pm 0.1°$. The data with more than 10 match-up observations were used for both the investigations of intersite and temporal variability. Ten TCCON sites (Burgos,

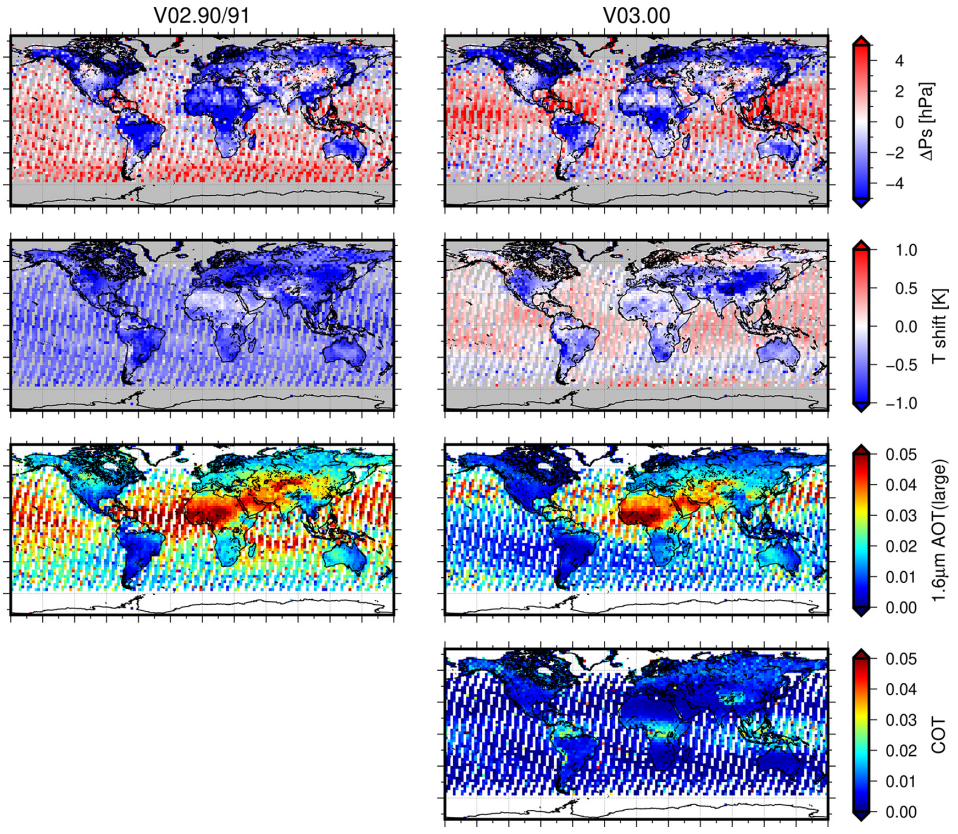

Figure 9. Distributions of the averaged ΔP_s, T shift, large particle AOT at 1.6 µm, and COT at 0.55 µm from V02.90/91 and V03.00. COT is obtainable only from V03.

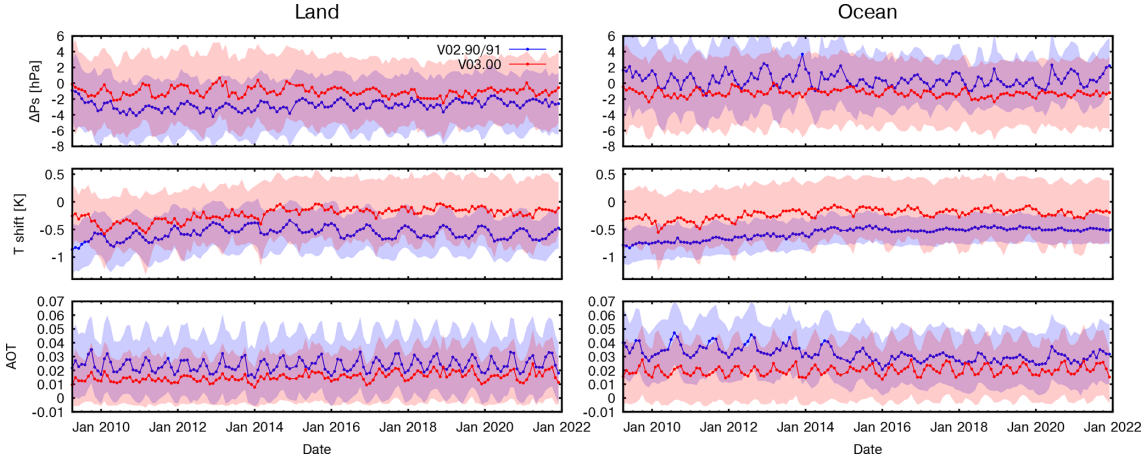

Figure 10. Time series of the monthly averaged ΔP_s, T shift, large particle AOT at 1.6 µm from V02.90/91 and V03.00. The shades show $\pm 1\sigma$.

Caltech, JPL02, Lauder02, Lauder03, Lamont, Paris, Saga, Sodankyla, and Tsukuba) were found as the match-up data sites for investigating intersite variability Site biases, average site bias, and site-to-site variability were calculated as the mean differences from TCCON for individual sites, an average of site biases, and a standard deviation of site biases, respectively. The average site biases and the site-to-site variabilities from V03.00 are −0.01 and 1.74 ppm for XCO_2 and −2.14 and 9.33 ppb for XCH_4, respectively. Those from V02.90/91 are −0.02 and 1.72 ppm for XCO_2 and 5.99 and 9.12 ppb for XCH_4. The average site biases and the site-to-site variabilities of XCO_2 are similar for V03.00

Table 6. Validation results of V03.00 and V02.90/91 against the TCCON measurements version GGG2020 with the match-up condition of ±2°. The mean values of the differences between TCCON and GOSAT (bias) and their standard deviations (SD) are shown for each combination of surface conditions and gain settings.

Version	Surface/gain	CO_2			CH_4		
		No. of data	Bias (ppm)	SD (ppm)	No. of data	Bias (ppb)	SD (ppb)
V02.90/91	Land/H	7357	−0.56	2.13	7365	2.97	11.94
	Land/M	1385	−0.79	1.89	1385	8.13	19.17
	Ocean/H	72	−1.63	2.62	72	5.60	15.43
V03.00	Land/H	8780	−0.61	2.20	8790	−4.23	11.97
	Land/M	1360	−0.88	1.97	1360	−0.19	19.29
	Ocean/H	61	−8.12	2.81	61	−9.71	14.60

Table 7. Validation results of V03.00 and V02.90/91 over land with gain H against the TCCON measurement version GGG2020 in the match-up condition of ±0.1°.

Version	CO_2			CH_4		
	No. of data	Bias (ppm)	SD (ppm)	No. of data	Bias (ppb)	SD (ppb)
V02.90/91	1743	−0.31	1.76	1744	4.81	9.81
V03.00	2111	−0.43	1.81	2112	−3.30	9.68

and V02.90/91. For XCH_4, although the site-to-site variability from V03.00 is slightly higher than that from V02.90/91, the average site bias is smaller in V03.00. Temporal variability was calculated from the annual mean of the differences between GOSAT and TCCON. The time series of the annual mean differences are shown in Fig. 11. Temporal trends of the XCO_2 from V03.00 and V02.90/91 are similar after 2014, although the values from V02.90/91 are respectively large in 2012 and 2013. Although the values from V03.00 are generally lower than those from V02.90/91, the same trends are found for XCH_4. The standard deviations of the annual mean values from V03.00 and V02.90/91 are 0.42 and 0.52 ppm for XCO_2 and 1.44 and 2.06 ppb for XCH_4, respectively. Thus, V03.00 exhibits smaller temporal variability than V02.90/91 in this analysis. The decadal trends of the differences from V02.90/91 and V03.00 are -0.63 ± 0.15 and -0.11 ± 0.1 ppm decade^{-1} for XCO_2 and -2.41 ± 0.84 and -0.37 ± 0.77 ppb decade^{-1} for XCH_4. The consistencies of the decadal trend are slightly improved in V03.00.

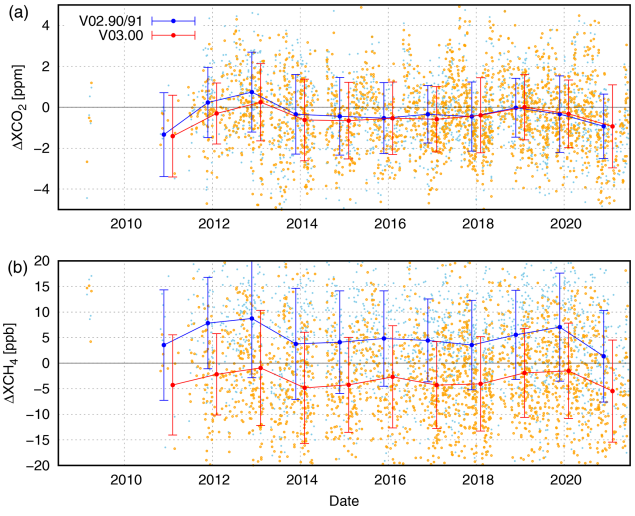

Figure 11. Annual mean differences of the GOSAT L2 product and TCCON GGG2020 in the match-up condition of ±0.1° for XCO_2 **(a)** and XCH_4 **(b)**. The red and blue lines indicate V03.00 and V02.90/91, respectively. The annual mean plots are slightly shifted between V02 and V03 for visibility. Each individual observation from V03.00 and V02.90/91 is plotted as orange and light-blue dots.

4.4 Evaluating the long-term trend using in situ measurements

The TCCON sites used in the previous section were mainly obtained over land. However, as noted in Sect. 2.2, there is an issue with the decadal growth rate of XCO_2 estimated using the V02.90/91 product over the ocean. In this section, we evaluate the long-term trends of XCO_2 using in situ measurement data.

NIES has observed CO_2 via air sampling on ships (Tohjima et al., 2005) and at ground stations (Nomura et al., 2017, 2021) in southwestern Asia and the western Pacific Ocean for more than a decade. CO_2 in the upper troposphere has been observed by aircraft in the CONTRAIL project (Machida et al., 2008). In addition, NOAA Global Monitoring Laboratory has provided flask sampling and in situ measurement data on the western Pacific islands (Conway et al.,

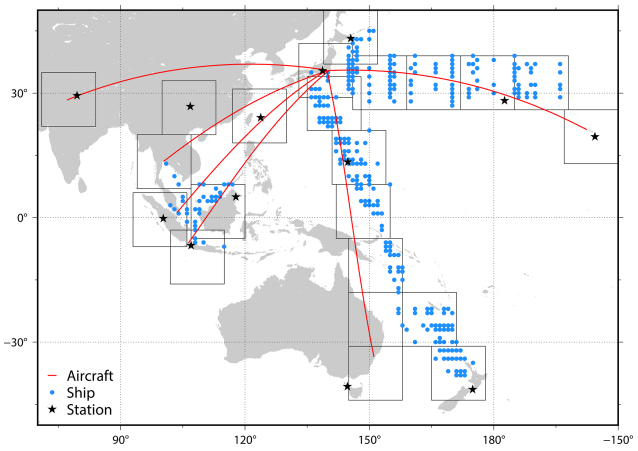

Figure 12. Main route or locations of the aircraft (red line), ship (blue dot), and station (black star) measurements. The areas for comparison with the GOSAT data are shown in boxes. Here, we only show the main routes of the aircraft measurements (Haneda/-Narita to Delhi, Bangkok, Singapore, Jakarta, Sydney, and Honolulu) accounting for more than 97 %, although the remaining data contain the other routes (Haneda/Narita to Taipei, Kuala Lumpur, Denpasar, Cairns, Brisbane, and Guam).

1994; Lan et al., 2022). The data used in this study are listed in Table B2. The products from these in situ measurements are appropriate to evaluate the GOSAT product in terms of the stability of data accuracy. Because these observations obtain the concentrations of the trace gases at the surfaces or at certain atmospheric levels that are not column-averaged, they are not directly comparable with the XCO_2 obtained from GOSAT. Therefore, we only focus on the decadal increasing trend of CO_2 from both products in this study. Further, we only evaluate the CO_2 trends, because the comparison of CH_4 is more complicated due to its large vertical gradient and variability. For aircraft measurement, only the data obtained at altitudes of 5 km or higher were used. The 22 areas are defined using $12° \times 12°$ grid boxes and the CO_2 concentrations obtained from GOSAT and each in situ measurement platform were monthly averaged in each area for comparison. The locations of the in situ measurements and areas used in this analysis are depicted in Fig. 12. The monthly averaged values in each area from GOSAT and the in situ measurements are directly compared to investigate the difference in the decadal growth.

Figure 13 shows the time series of the differences between the XCO_2 from the GOSAT V02.90/91 or V03.00 product and CO_2 concentration from each in situ measurement platform. Here we used the data until 2020. The trend is estimated by the least squared linear regression from the scatter data. Over land, the growth rates of CO_2 estimated from the GOSAT V02.90/91 and V03.00 products are consistent with that from the in situ measurements within 1 ppm decade^{-1}. This value is close to the difference between TCCON and the in situ measurements. On the other hand, the growth rate

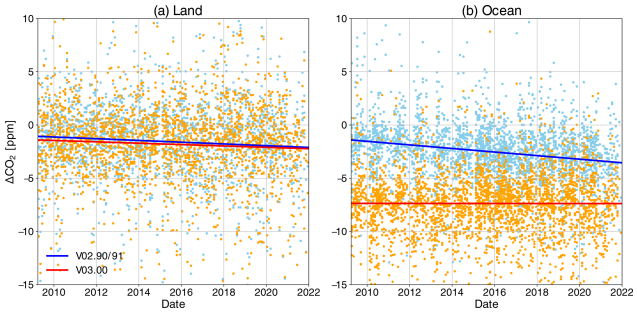

Figure 13. Time series of the differences between the GOSAT products and in situ measurements (GOSAT minus in situ measurements) over land **(a)** and the ocean **(b)**. The regression lines are plotted as red and blue lines.

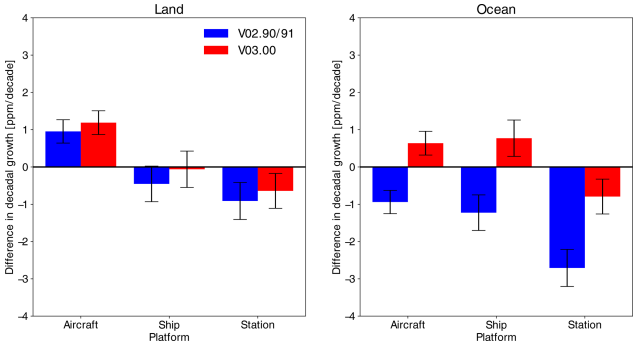

Figure 14. Differences in the decadal growths of CO_2 between the GOSAT product and each in situ measurement platform.

for V02.90/01 over the ocean is 1.68 ± 0.14 ppm decade^{-1} smaller than that from the in situ measurements. However, the difference in the growth rate for V03.00 is improved to 0.01 ± 0.15 ppm decade^{-1}, although the biases are negatively large, as shown in the previous sections. The differences in the growth rates between GOSAT and each platform are shown in Fig. 14. Over land, the absolute differences in the growth rates from V03.00 are smaller than those from V02.90/91 for ship and station measurements, although they are slightly larger for aircraft. Over the ocean, the differences from V03.00 are smaller than those from V02.90/91 for all platforms. In particular, the large discrepancy of -2.7 ppm decade^{-1} with the station measurement in the V02.90/91 product was improved to -0.8 ppm decade^{-1} in the V03.00 product.

The main cause of this trend of the GOSAT V02.90/91 product over the ocean is estimated as the sensitivity degradation of TANSO–FTS. Although the degradation is considered in the V02 algorithm with the degradation model according to Yoshida et al. (2012), the degradations after 2012 are the expected ones. The error of this degradation model generates a gap in the spectral baseline between the observed and simulated spectra. The difference in trend is not significant over land because the gap can be adjusted by simulta-

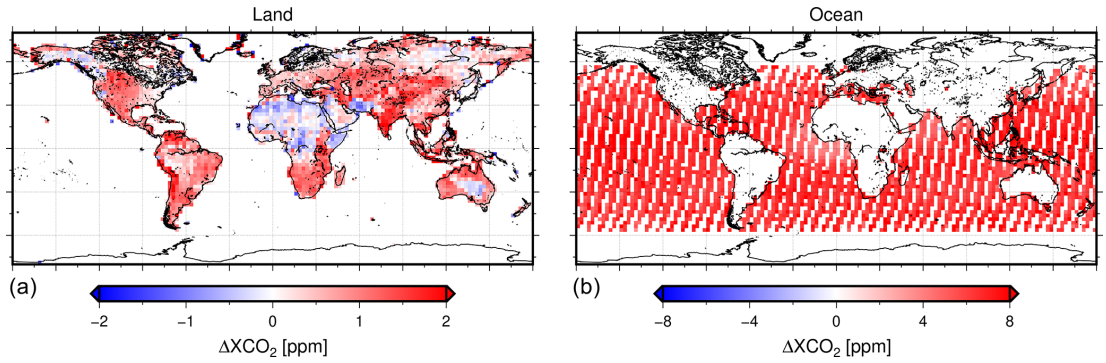

Figure 15. Difference of XCO_2 between V03.00 and bias-corrected one (bias-corrected minus V03.00) over land **(a)** and the ocean **(b)**, averaged from the launch to 2021 within 2.5° × 2.5° grid boxes.

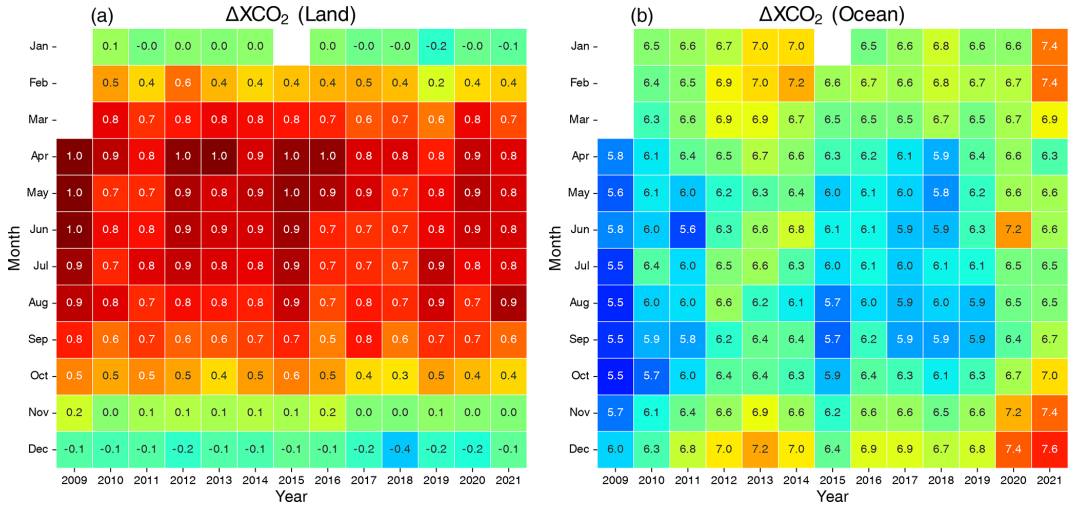

Figure 16. Time series heat maps of the monthly mean changes of XCO_2 by the bias correction over land **(a)** and the ocean **(b)**. The color scales differ for the panels.

neously retrieving surface albedo. In the NIES retrieval algorithm, only the wind speed is retrieved as a surface property over the ocean and not surface albedo. Therefore, the difference in the trend of CO_2 between GOSAT V02.90/91 and the in situ measurements could have resulted from the increasing error of the degradation model with time. This improvement of the trend of V03.00 over the ocean is mainly because of the update of the degradation model described in Sect. 3.2, as the other updates do not vary over time.

4.5 Bias correction

Because the V03.00 product has biases particularly for XCO_2 over the ocean, as shown in the previous sections, those should be corrected. We used TCCON GGG2014 for this bias correction because insignificant changes were found in XCO_2 between both versions and the available amount of data is larger than GGG2020. The site information of TCCON GGG2014 used in this study is listed in Table B3. The bias correction for XCH_4 is not processed here, since those are largely changed between GGG2014 and GGG2020. Since the GGG2020 is not fully available, we plan to correct XCH_4 based on GGG2020 after more stations are published. The bias-correction strategy is the same as that used in the V02.95/96 and V02.97/98 products (NIES GOSAT project, 2020). The bias correction of the XCO_2 for V03 is a function of AOT, ΔP_s, and surface albedo at the O_2 A sub-band. Multiple linear regression analysis was used to estimate the coefficients. The TCCON data from 2009 to 2019 are used as the reference data. The changes in the XCO_2 from V03.00 after the correction are shown in Fig. 15. Over land, the corrections are generally positive, although they are negative only in the high reflectance surface areas such as the Sahara and Australia. The corrections over the ocean show similar positive values globally. The negative bias over the ocean revealed in the previous sections is corrected by this procedure. The mean changes and their standard deviations in XCO_2 by the bias correction are +0.55 ppm over land and +6.44 ppm over the ocean. The time series of the monthly mean changes

by the bias correction is depicted in Fig. 16. The seasonal dependencies of the correction differ for the surface. Over land, the correction magnitude is large in boreal spring and summer. On the other hand, it is large in boreal winter over the ocean. This is because the ancillary parameters used in the bias correction are different from the surfaces, and the common parameters also have different seasonal variations from the surfaces as shown in Fig. 10. The bias-corrected version of the XCO_2 product is planned to be released as V03.05.

5 Summary and conclusions

The retrieval algorithm for the GOSAT TANSO–FTS SWIR L2 product from NIES was updated to generate the next version; the V03 product. The main changes in the V03 algorithm compared with the current retrieval algorithm (V02) are as follows:

1. COT and CTP are retrieved simultaneously with the GHGs instead of the cirrus cloud screening using the 2 µm band in the pre-screening processing.

2. The degradation model of TANSO–FTS is updated to that of Someya and Yoshida (2020).

3. Solar irradiance spectra are updated to those produced from TSIS-1 HSRS and the version 2016 of Toon (2015b).

4. Gas absorption coefficient tables are updated using several new references.

The retrieval results show that the spectral fitting accuracies are successfully improved, and the systematic spectral residuals in the V02.90/91 product are reduced in the O_2 A, WCO_2, and CH_4 sub-bands. Conversely, the residual in the SCO_2 sub-band increases over the ocean with a systematic spectral structure corresponding to the CO_2 absorptions. This increase in the residual is mainly attributed to spectral biases at baseline between observed and simulated spectra.

The amount of data from V03.00 is larger than that from V02.90/91 over land and the mixed surfaces mainly owing to the change in the treatment of clouds, although it is smaller over the ocean because of the residual in the SCO_2 sub-band. Overall, the amount of data from V03.00 increased by 2.3 % compared with that from V02.90/91.

The direct comparison of V03.00 with V02.90/91 and the validation using TCCON measurements shows that the quality of XCO_2 from V03.00 is almost the same level as that from V02.90/91 over land – the update achieves an increase in the available data without reducing the quality of the retrieved XCO_2. On the other hand, the XCO_2 from V03.00 over the ocean is negatively biased and the bias correction is necessary. Although the bias XCH_4 over land with gain H from V03.00 is slightly larger than that from V02.90/91 in the match-up condition of $\pm 2°$, it is smaller in the stricter condition, $\pm 0.1°$. Regarding the spatial variability in CH_4, the results obtained with the stricter match-up condition are more reliable, and V03.00 improves the quality of XCH_4. The standard deviations of the XCH_4 differences between GOSAT and TCCON are similar for V02.90/91 and V03.00. Considering these validation results and the improvement in fitting accuracies, the quality of the XCH_4 from V03.00 is comparable to or better than that from V02.90/91. In addition, the investigation of site-to-site and temporal variability of XCO_2 and XCH_4 biases from V03.00 demonstrates that their site-to-site variabilities are approximately the same level and the temporal variabilities are slightly smaller than those from V02.90/91.

The long-term trends of XCO_2 from both product versions are evaluated via in situ measurements. The V03.00 product resolves the issue that the decadal CO_2 growth rate estimated from the V02.90/91 products over the ocean is 1.7 ppm decade^{-1} lower than that from the in situ measurements.

Although the V03 retrieval algorithm has an issue to be resolved for XCO_2 over the ocean, the objectives of the update, increase in data, and improvement of the fitting accuracy are generally achieved over land. Notably, the increase in data of 13 % over land and the improvements of the temporal variabilities of biases are helpful for the flux inversions or emission estimates of CO_2 and CH_4. NIES plans to release the L2 V03.00 product and the bias-corrected V03.05 in near future.

Appendix A: Sensitivity analysis for updated items

Table A1. Applied updated items (1–4) for sensitivity test retrievals (A–E).

	1	2	3	4
A	x	x	x	x
B		x	x	x
C			x	x
D		x		x
E		x	x	

Although the updated items do not independently affect the retrieval results of V03 and it is difficult to evaluate separately, we performed some sensitivity test retrievals in order to investigate the changes in retrieval results from each updated item as a reference. Updated items are categorized as follows:

1. Cirrus properties are added to the state vector instead of the cirrus cloud screening using the 2 µm band.

2. The degradation model is replaced.

3. Solar irradiance spectra are replaced.

Table A2. Summary of sensitivity test retrieval results.

		No. of data	XCO_2 (ppm)	XCH_4 (ppb)	ΔP_s (hPa)	T shift (K)	AOT (large)
Land	A	188683	396.79	1797.67	−1.95	−0.37	0.020
	B	171 359	396.65	1795.96	−2.06	−0.24	0.024
	C	170 224	397.31	1798.77	−3.70	−0.23	0.024
	D	170 393	396.33	1802.86	−0.73	−0.26	0.024
	E	158 166	396.56	1794.53	−2.33	−0.74	0.023
Ocean	A	75 165	393.87	1790.36	1.34	0.18	0.019
	B	56 869	393.53	1788.49	0.86	0.17	0.015
	C	14	393.19	1795.57	−5.15	−0.09	0.026
	D	34 059	401.80	1805.63	2.53	−0.19	0.024
	E	19 847	393.26	1802.44	0.89	−0.75	0.027

4. Gas absorption coefficient tables and the empirical noise model are replaced.

The sensitivity test retrievals were performed by changing the items updated from V02.90/91 for six patterns (A–E), as listed in Table A1. The thresholds of the spectral residuals in the post-screening are the same as that of V03. Since all the items are updated, A is equal to the V03.00 product. Of all the data until May 2020, 20 % are processed because of the computational costs. The results of the retrievals are summarized in Table A2.

The retrieval patterns A and B show similar spectral residuals (not shown), and the cirrus cloud treatment seems to have fewer impacts on the residuals. AOT of a large particle at 1.6 µm over land and temperature shift in high altitudes estimated from A are smaller than those from B. The retrieval tests C, D, and E are compared with B to estimate the effects of items 2, 3, and 4 in the following.

C is the retrieval test that changes the degradation model to the old one from B. In this retrieval, few products are available over the ocean because the normalized mean squared residuals in the O_2 A and SCO_2 sub-bands are > 2, and data are rejected in the post-screening in most observations. The residuals in the WCO_2 sub-band are also larger than those from B. These are because there are large differences in the baselines of the previous and updated solar irradiance spectra. The degradation models include the absolute degradation factor which adjusts the baseline of the calculated and observed spectra. Although the absolute degradation factor is estimated using the updated solar irradiance in the updated degradation model, that is done using the old solar irradiance spectra in the old degradation model. It is estimated that the residuals in the O_2 A sub-band are increased along with the change of the retrieved XCO_2 due to the residuals in the SCO_2 sub-band.

The number of data over the ocean from D is decreased because of the same reason as C. XCH_4 from D is approximately 7 ppb larger than that from B over land. Over the ocean, XCO_2 significantly changed. Since there are no significant differences in the number of data in time over the ocean, this implies that the update of solar irradiance has significant impacts on XCO_2. AOT over the ocean from D is larger than that from B.

The changes in temperature shift are largest in E. Especially, it is 1 K smaller than that from B over the ocean, and the averaged values are negative globally, similar to those from V02.90/91. Although there is a difference in XCH_4 between E and B over the ocean, this is not seen over land. Therefore, the update of the absorption coefficient may have a less direct impact on XCH_4.

Based on the retrieval results, the update of solar irradiance spectra seems to have a relatively large impact on the XCH_4 because of the significant change over land. The update of the degradation model also impacts ΔP_s in the same way as solar irradiance, but has less impact on XCH_4. Large particle AOT is mainly affected by the updates in the treatment of cirrus clouds over land.

Over the ocean, it is very difficult to estimate the causes of the changes in the results because the numbers of data are significantly different for each pattern. However, XCO_2 is significantly changed by the update of solar irradiance. AOT estimated from C, D, and E are changed from that from B, so that the changes of AOT are multiply affected by the updates. Temperature shift seems to be largely affected by the updates of the absorption coefficient table over both surfaces.

Appendix B: Information of TCCON and in situ measurement data

Site information of each TCCON data used for validation and bias correction is listed in Tables B1 and B3. Data availabilities and citations of in situ measurements are listed in Table B2.

Table B1. Site information of the TCCON GGG2020 data used for validation.

Site	Latitude	Longitude	Start date	End date	Reference
Bremen	53.10° N	8.85° E	6 Jan 2009	24 Jun 2021	Notholt et al. (2022)
Burgos	18.533° N	120.650° E	3 Mar 2007	30 Apr 2020	Morino et al. (2022a)
Caltech (Pasadena)	34.136° N	118.127° W	20 Sep 2012	1 Mar 2022	Wennberg et al. (2022a)
East Trout Lake	54.354° N	104.987° W	3 Oct 2016	6 Mar 2022	Wunch et al. (2022)
Four Corners	36.707° N	108.48° W	16 Mar 2013	3 Oct 2013	Dubey et al. (2022a)
Indianapolis	39.861° N	86.004° W	23 Aug 2012	1 Dec 2012	Iraci et al. (2022)
JPL02	34.202° N	118.175° W	19 May 2011	14 May 2018	Wennberg et al. (2022b)
Karlsruhe	49.100° N	8.439° E	15 Jan 2014	22 Dec 2021	Hase et al. (2022)
Lauder01	45.038° S	169.684° E	28 Jan 2004	19 Feb 2010	Sherlock et al. (2022a)
Lauder02	45.038° S	169.684° E	2 Jan 2013	30 Sep 2018	Sherlock et al. (2022b)
Lauder03	45.038° S	169.684° E	2 Oct 10 2018	30 Mar 2021	Pollard et al. (2022)
Lamont	36.604° N	97.486° W	6 Jul 2008	27 Feb 2022	Wennberg et al. (2022c)
Manaus	3.213° S	60.598° W	30 Sep 2014	27 Jul 2015	Dubey et al. (2022b)
Nicosia	35.141° N	33.381° E	3 Sep 2019	1 Jun 2021	Petri et al. (2022)
Orleans	47.97° N	2.113° E	29 Aug 2009	8 Mar 2021	Warneke et al. (2022)
Paris	48.846° N	2.356° E	23 Sep 2014	16 Jun 2021	Té et al. (2022)
Park Falls	45.945° N	90.273° W	26 May 2004	218 Feb 2022	Wennberg et al. (2022d)
Reunion	20.901° S	55.485° E	1 Mar 2015	18 Jul 2020	De Mazière et al. (2022)
Rikubetsu	43.457° N	143.766° E	24 Jun 2014	30 Jun 2021	Morino et al. (2022b)
Saga	33.241° N	130.288° E	28 Jul 2011	30 Jun 2021	Shiomi et al. (2022)
Sodankyla	67.367° N	26.631° E	5 Mar 2018	18 Oct 2021	Kivi et al. (2022)
Tsukuba	36.051° N	140.122° E	28 Mar 2014	28 Jun 2021	Morino et al. (2022c)
Xianghe	39.75° N	116.96° E	14 Jun 2018	30 Nov 2021	Zhou et al. (2022)

Table B2. In situ measurement data availability.

Platform/site	Citation
Aircraft	Atmospheric CO_2 mole fraction data of CONTRAIL-CME; https://doi.org/10.17595/20180208.001
Ship	https://soop.jp (last access: 13 March 2023) (partially on request)
NIES station	
Ochi-ishi	Continuous observational data of atmospheric CO_2 mixing ratios at Cape Ochi-ishi; https://doi.org/10.17595/20160901.002
Mt. Fuji	Daily observational data of atmospheric CO_2 mixing ratios at the summit of Mt. Fuji; https://doi.org/10.17595/20170616.001
Nainital	Atmospheric Carbon Dioxide Dry Air Mole Fraction at Nainital, India, https://doi.org/10.17595/20220301.001
Hateruma	Continuous observational data of atmospheric CO_2 mixing ratios on Hateruma Island; https://doi.org/10.17595/20160901.001
Guiyang	On request
Danum Valley	On request
Bukit Kototabang	On request
Serpong	On request
Bogor	On request
Cibeureum	On request
NOAA flask/in situ	Atmospheric carbon dioxide dry air mole fractions from the NOAA GML carbon cycle cooperative global air sampling network, 1968–2021, Version: 28 Jul 2022; https://doi.org/10.15138/wkgj-f215
Midway	Atmospheric carbon dioxide dry air mole fractions at Sand Island, Midway; https://gml.noaa.gov/aftp/data/trace_gases/co2/flask/surface/txt/co2_mid_surface-flask_1_ccgg_month.txt (last access: 13 March 2023)
Guam	Atmospheric carbon dioxide dry air mole fractions at Mariana Islands, Guam; https://gml.noaa.gov/aftp/data/trace_gases/co2/flask/surface/txt/co2_gmi_surface-flask_1_ccgg_month.txt (last access: 13 March 2023)
Cape Grim	Atmospheric carbon dioxide dry air mole fractions at Cape Grim, Tasmania; https://gml.noaa.gov/aftp/data/trace_gases/co2/flask/surface/txt/co2_cgo_surface-flask_1_ccgg_month.txt (last access: 13 March 2023)
Baring Head	Atmospheric carbon dioxide dry air mole fractions at Baring Head, New Zealand; https://gml.noaa.gov/aftp/data/trace_gases/co2/flask/surface/txt/co2_bhd_surface-flask_1_ccgg_month.txt (last access: 13 March 2023)

Table B3. Site information of the TCCON GGG2014 data used for bias correction.

Site	Latitude	Longitude	Start date	End date	Reference
Ascension	7.916° S	14.333° W	22 May 2012	31 Oct 2018	Feist et al. (2014)
Anmeyondo	36.538° N	126.331° E	2 Feb 2015	18 Apr 2018	Goo et al. (2014)
Bialystok	53.23° N	23.025° E	1 Mar 2009	1 Oct 2018	Deutscher et al. (2015)
Bremen	53.10° N	8.85° E	22 Jan 2010	24 Feb 2021	Notholt et al. (2014)
Burgos	18.533° N	120.650° E	3 Mar 2017	31 Mar 2020	Morino et al. (2018a)
Caltech (Pasadena)	34.136° N	118.127° W	20 Sep 2012	29 Dec 2020	Wennberg et al. (2015)
Darwin	12.425° S	130.892° E	28 Aug 2005	30 Apr 2020	Griffith et al. (2014a)
East Trout Lake	54.354° N	104.987° W	7 Oct 2016	6 Sep 2020	Wunch et al. (2017)
Edwards	34.958° N	117.882° W	20 Jul 2013	31 Dec 2020	Iraci et al. (2016a)
Eureka	80.05° N	86.42° W	24 Jul 2010	6 Jul 2020	Strong et al. (2017)
Four Corners	36.707° N	108.480° W	16 Mar 2013	4 Oct 2013	Dubey et al. (2014a)
Garmisch	47.476° N	11.063° E	16 Jul 2007	1 Apr 2021	Sussmann and Rettinger (2015)
Hefei	31.91° N	117.17° E	18 Sep 2015	23 Oct 2018	Liu et al. (2018)
Indianapolis	39.861° N	86.004° W	23 Aug 2012	1 Dec 2012	Iraci et al. (2016b)
JPL02	34.202° N	118.175° W	19 May 2011	14 May 2018	Wennberg et al. (2016a)
Karlsruhe	49.100° N	8.439° E	19 Apr 2010	22 Dec 2021	Hase et al. (2015)
Lauder01	45.038° S	169.684° E	29 Jun 2004	9 Dec 2010	Sherlock et al. (2014a)
Lauder02	45.038° S	169.684° E	2 Feb 2010	31 Oct 2018	Sherlock et al. (2014b)
Lauder03	45.038° S	169.684° E	3 Oct 2018	31 Dec 2020	Pollard et al. (2019)
Lamont	36.604° N	97.486° W	6 Jul 2008	28 Dec 2020	Wennberg et al. (2016b)
Manaus	3.213° S	60.598° W	1 Oct 2014	24 Jun 2015	Dubey et al. (2014b)
Nicosia	35.141° N	33.381° E	31 Aug 2019	9 Mar 2021	Petri et al. (2022)
Orleans	47.97° N	2.113° E	29 Aug 2009	8 Mar 2021	Warneke et al. (2014)
Paris	48.846° N	2.356° E	23 Sep 2014	22 Jun 2020	Té et al. (2014)
Park Falls	45.945° N	90.273° W	2 Jun 2004	29 Dec 2020	Wennberg et al. (2017)
Reunion	20.901° S	55.485° E	16 Sep 2011	18 Jul 2020	De Mazière et al. (2014)
Rikubetsu	43.457° N	143.766° E	16 Nov 2013	30 Sep 2019	Morino et al. (2016)
Saga	33.241° N	130.288° E	28 Jul 2011	29 Dec 2020	Kawakami et al. (2014)
Sodankyla	67.367° N	26.631° E	16 May 2009	20 Oct 2020	Kivi et al. (2017)
Tsukuba	36.051° N	140.122° E	4 Aug 2011	30 Sep 2019	Morino et al. (2018b)
Wollongong	34.406S°	150.879° E	26 Jun 2008	30 Jun 2020	Griffith et al. (2014b)
Zugspitze	47.42° N	10.98° E	24 Apr 2015	1 Apr 2021	Sussmann and Rettinger (2018)

Data availability. The GOSAT SWIR L2 products are available from the GOSAT Data Archive Service (https://data2.gosat.nies.go.jp/index_en.html, last access: 13 March 2023; GOSAT, 2023). The TCCON data are available from the TCCON Data Archive (https://tccondata.org, last access: 13 March 2023; TCCON, 2023). The availabilities of the in situ measurement data used in this paper are listed in Table B2.

Supplement. The supplement related to this article is available online at: https://doi.org/10.5194/amt-16-1477-2023-supplement.

Author contributions. YS performed the investigation of the retrieval results, contributed to the development of the retrieval system, and prepared the paper. YY designed and developed the retrieval system, contributed to the investigation of the retrieval results, and edited the paper. HO and IM contributed to the development of the retrieval system and provided the TCCON data. SN, AK, and HM contributed to the investigation of the retrieval results. TM acquired funding. JL, VV, BH, YT, MS, RK, MZ, YO, ND, and DG contributed in providing the TCCON data. All the co-authors reviewed the paper.

Competing interests. At least one of the (co-)authors is a member of the editorial board of *Atmospheric Measurement Techniques*. The peer-review process was guided by an independent editor, and the authors also have no other competing interests to declare.

Disclaimer. Publisher's note: Copernicus Publications remains neutral with regard to jurisdictional claims in published maps and institutional affiliations.

Acknowledgements. We acknowledge TCCON, CONTRAIL, and NOAA Global Monitoring Network for making the data available to the public.

Financial support. This work has been supported by the NIES GOSAT project. A portion of the TCCON data development was carried out at the Jet Propulsion Laboratory, California Institute of Technology, under a contract with the National Aeronautics and Space Administration (grant no. 80NM0018D0004). The TCCON stations at Rikubetsu, Tsukuba, and Burgos are supported in part by the GOSAT series project. Local support for Burgos is provided by the Energy Development Corporation (EDC, Philippines). The Paris TCCON site has received funding from Sorbonne Université, the French National Centre for Scientific Research, CNRS, the French National Centre for Space Studies, CNES (ICOS-AtmoSat project), and Région Île-de-France. The TCCON site at Réunion Island has been operated by the Royal Belgian Institute for Space Aeronomy with financial support since 2014 by the EU project ICOS-Inwire and the ministerial decree for ICOS (FR/35/IC1 to FR/35/C6), and local activities are supported by LACy/UMR8105 and OSU-R/UMS3365 – Université de La Réunion". The Anmyendo TCCON site is funded by the Korea Meteorological Administration Research and Development Program (grant nos. KMA2018-00522 and KMI2022-01610).

Review statement. This paper was edited by Joanna Joiner and reviewed by T. E. Taylor and one anonymous referee.

References

Baum, B. A., Yang, P., Heymsfield, A. J., Schmitt, C. G., Xie, Y., Bansemer, A., Hu, Y.-X. and Zhang, Z.: Improvements in Shortwave Bulk Scattering and Absorption Models for the Remote Sensing of Ice Clouds, J. Appl. Meteorol. Climatol., 50, 1037–1056, https://doi.org/10.1175/2010JAMC2608.1, 2011.

Butz, A., Guerlet, S., Hasekamp, O., Schepers, D., Galli, A., Aben, I., Frankenberg, C., Hartmann, J.-M., Tran, H., Kuze, A., Keppel-Aleks, G., Toon, G., Wunch, D., Wennberg, P., Deutscher, N., Griffith, D., Macatangay, R., Messerschmidt, J., Notholt, J., and Warneke, T.: Toward accurate CO_2 and CH_4 observations from GOSAT, Geophys. Res. Lett., 38, L14812, https://doi.org/10.1029/2011GL047888, 2011.

Coddington, O. M., Richard, E. C., Harber, D., Pilewskie, P., Woods, T. N., Chance, K., Liu, X., and Sun, K.: The TSIS-1 Hybrid Solar Reference Spectrum, Geophys. Res. Lett., 48, e2020GL091709, https://doi.org/10.1029/2020GL091709, 2021.

Cogan, A. J., Boesch, H., Parker, R. J., Feng, L., Palmer, P. I., Blavier, J.-F. L., Deutscher, N. M., Macatangay, R., Notholt, J., Roehl, C., Warneke, T., and Wunch, D.: Atmospheric carbon dioxide retrieved from the Greenhouse gases Observing SATellite (GOSAT): Comparison with ground-based TCCON observations and GEOS-Chem model calculations, J. Geophys. Res.-Atmos., 117, D21301, https://doi.org/10.1029/2012JD018087, 2012.

Conway, T. J., Tans, P. P., Waterman, L. S., Thoning, K. W., Kitzis, D. R., Masarie, K. A., and Zhang, N.: Evidence for interannual variability of the carbon cycle from the National Oceanic and Atmospheric Administration/Climate Monitoring and Diagnostics Laboratory Global Air Sampling Network, J. Geophys. Res.-Atmos., 99, 22831–22855, https://doi.org/10.1029/94JD01951, 1994.

De Mazière, M., Sha, M. K., Desmet, F., Hermans, C., Scolas, F., Kumps, N., Metzger, J.-M., Duflot, V., and Cammas, J.-P.: TCCON data from Reunion Island (RE), Release GGG2014R0, https://doi.org/10.14291/tccon.ggg2014.reunion01.R0/1149288, 2014.

De Mazière, M., Sha, M. K., Desmet, F., Hermans, C., Scolas, F., Kumps, N., Metzger, J.-M., Duflot, V., and Cammas, J.-P.: TCCON data from Réunion Island (RE), Release GGG2020.R0, https://doi.org/10.14291/tccon.ggg2020.reunion01.R0, 2022.

Deutscher, N. M., Notholt, J., Messerschmidt, J., Weinzierl, C., Warneke, T., Petri, C., and Grupe, P.: TCCON data from Bialystok (PL), Release GGG2014.R1, https://doi.org/10.14291/TCCON.GGG2014.BIALYSTOK01, 2015.

Devi, V. M., Benner, D. C., Sung, K., Crawford, T. J., Yu, S., Brown, L. R., Smith, M. A. H., Mantz, A. W., Boudon, V., and Ismail, S.: Self- and air-broadened line shapes in the $2\nu 3$

P and R branches of $^{12}CH_4$, J. Mol. Spectrosc., 315, 114–136, https://doi.org/10.1016/j.jms.2015.05.003, 2015.

Devi, V. M., Benner, D. C., Sung, K., Brown, L. R., Crawford, T. J., Yu, S., Smith, M. A. H., Mantz, A. W., Boudon, V., and Ismail, S.: Spectral line parameters including line shapes in the $2\nu3$ Q branch of $^{12}CH_4$, J. Quant. Spectrosc. Radiat. Transf., 177, 152–169, https://doi.org/10.1016/j.jqsrt.2015.12.009, 2016.

Drouin, B. J., Benner, D. C., Brown, L. R., Cich, M. J., Crawford, T. J., Devi, V. M., Guillaume, A., Hodges, J. T., Mlawer, E. J., Robichaud, D. J., Oyafuso, F., Payne, V. H., Sung, K., Wishnow, E. H., and Yu, S.: Multispectrum analysis of the oxygen A-band, J. Quant. Spectrosc. Radiat. Transf., 186, 118–138, https://doi.org/10.1016/j.jqsrt.2016.03.037, 2017.

Dubey, M., Lindenmaier, R., Henderson, B., Green, D., Allen, N., Roehl, C., Blavier, J.-F., Butterfield, Z., Love, S., Hamelmann, J., and Wunch, D.: TCCON data from Four Corners (US), Release GGG2014R0, https://doi.org/10.14291/tccon.ggg2014.fourcorners01.R0/1149272, 2014a.

Dubey, M., Henderson, B., Green, D., Butterfield, Z., Keppel-Aleks, G., Allen, N., Blavier, J.-F., Roehl, C., Wunch, D., and Lindenmaier, R.: TCCON data from Manaus (BR), Release GGG2014R0, https://doi.org/10.14291/tccon.ggg2014.manaus01.R0/1149274, 2014b.

Dubey, M. K., Lindenmaier, R., Henderson, B. G., Allen, N. T., Roehl, C. M., Blavier, J.-F., Love S., and Wunch, D.: TCCON data from Four Corners (US), Release GGG2020.R0, https://doi.org/10.14291/tccon.ggg2020.fourcorners01.R0, 2022a.

Dubey, M. K., Henderson, B. G., Allen, N. T., Blavier, J.-F., Roehl, C. M., and Wunch, D.: TCCON data from Manaus (BR), Release GGG2020.R0, https://doi.org/10.14291/tccon.ggg2020.manaus01.R0, 2022b.

Feist, D. G., Arnold, S. G., John, N., and Geibel, M. C.: TCCON data from Ascension Island (SH), Release GGG2014R0, https://doi.org/10.14291/tccon.ggg2014.ascension01.R0/1149285, 2014.

Goo, T.-Y., Oh, Y.-S. and Velazco, V. A.: TCCON data from Anmeyondo (KR), Release GGG2014R0, https://doi.org/10.14291/tccon.ggg2014.anmeyondo01.R0/1149284, 2014.

Gordon, I. E., Rothman, L. S., Hill, C., Kochanov, R. V, Tan, Y., Bernath, P. F., Birk, M., Boudon, V., Campargue, A., Chance, K. V, Drouin, B. J., Flaud, J.-M., Gamache, R. R., Hodges, J. T., Jacquemart, D., Perevalov, V. I., Perrin, A., Shine, K. P., Smith, M.-A. H., Tennyson, J., Toon, G. C., Tran, H., Tyuterev, V. G., Barbe, A., Császár, A. G., Devi, V. M., Furtenbacher, T., Harrison, J. J., Hartmann, J.-M., Jolly, A., Johnson, T. J., Karman, T., Kleiner, I., Kyuberis, A. A., Loos, J., Lyulin, O. M., Massie, S. T., Mikhailenko, S. N., Moazzen-Ahmadi, N., Müller, H. S. P., Naumenko, O. V, Nikitin, A. V, Polyansky, O. L., Rey, M., Rotger, M., Sharpe, S. W., Sung, K., Starikova, E., Tashkun, S. A., Auwera, J. Vander, Wagner, G., Wilzewski, J., Wcisło, P., Yu, S., and Zak, E. J.: The HITRAN2016 molecular spectroscopic database, J. Quant. Spectrosc. Radiat. Transf., 203, 3–69, https://doi.org/10.1016/j.jqsrt.2017.06.038, 2017.

GOSAT: GOSAT Data Archive Service, GOSAT [data set], https://data2.gosat.nies.go.jp/index_en.html, last access: 13 March 2023.

Griffith, D. W. T., Deutscher, N. M., Velazco, V. A., Wennberg, P. O., Yavin, Y., Aleks, G. K., Washenfelder, R. a., Toon, G. C., Blavier, J.-F., Murphy, C., Jones, N., Kettlewell, G., Connor, B. J., Macatangay, R., Roehl, C., Ryczek, M., Glowacki, J., Culgan, T., and Bryant, G.: TCCON data from Darwin (AU), Release GGG2014R0, https://doi.org/10.14291/tccon.ggg2014.darwin01.R0/1149290, 2014a.

Griffith, D. W. T., Velazco, V. A., Deutscher, N. M., Murphy, C., Jones, N., Wilson, S., Macatangay, R., Kettlewell, G., Buchholz, R. R., and Riggenbach, M.: TCCON data from Wollongong (AU), Release GGG2014R0, https://doi.org/10.14291/tccon.ggg2014.wollongong01.R0/1149291, 2014b.

Hase, F., Blumenstock, T., Dohe, S., Groß, J., and Kiel, M. Ä.: TCCON data from Karlsruhe (DE), Release GGG2014.R1, https://doi.org/10.14291/tccon.ggg2014, 2015.

Hase, F., Herkommer, B., Groß, J., Blumenstock, T., Kiel, M. Ä., and Dohe: TCCON data from Karlsruhe (DE), Release GGG2020.R0, https://doi.org/10.14291/tccon.ggg2020.karlsruhe01.R0, 2022.

Iraci, L. T., Podolske, J., Hillyard, P. W., Roehl, C., Wennberg, P. O., Blavier, J.-F., Allen, N., Wunch, D., Osterman, G. B., and Albertson, R.: TCCON data from Edwards (US), Release GGG2014R1, https://doi.org/10.14291/tccon.ggg2014.edwards01.R1/1255068, 2016a.

Iraci, L. T., Podolske, J., Hillyard, P. W., Roehl, C., Wennberg, P. O., Blavier, J.-F., Landeros, J., Allen, N., Wunch, D., Zavaleta, J., Quigley, E., Osterman, G. B., Barrow, E., and Barney, J.: TCCON data from Indianapolis (US), Release GGG2014R1, https://doi.org/10.14291/tccon.ggg2014.indianapolis01.R1/1330094, 2016b.

Iraci, L. T., Podolske, J. R., Hillyard, P. W., Roehl, C., Wennberg, P. O., Blavier, J.-F., Landeros, J., Allen, N., Wunch, D., Zavaleta, J., Quigley, E., Osterman, G. B., Barrow, E., and Barney, J.: TCCON data from Indianapolis (US), Release GGG2020.R0, https://doi.org/10.14291/tccon.ggg2020.indianapolis01.R0, 2022.

Kawakami, S., Ohyama, H., Arai, K., Okumura, H., Taura, C., Fukamachi, T., and Sakashita, M.: TCCON data from Saga (JP), Release GGG2014R0, https://doi.org/10.14291/tccon.ggg2014.saga01.R0/1149283, 2014.

Kikuchi, N., Yoshida, Y., Uchino, O., Morino, I., and Yokota, T.: An advanced retrieval algorithm for greenhouse gases using polarization information measured by GOSAT TANSO-FTS SWIR I: Simulation study, J. Geophys. Res. Atmos., 121, 13113–129157, https://doi.org/10.1002/2015JD024720, 2016.

Kivi, R., Heikkinen, P., and Kyrö, E.: TCCON data from Sodankylä (FI), Release GGG2014.R0, https://doi.org/10.14291/tccon.ggg2014.sodankyla01.R0/1149280, 2017.

Kivi, R., Heikkinen, P., and Kyrö, E.: TCCON data from Sodankylä (FI), Release GGG2020.R0, https://doi.org/10.14291/tccon.ggg2020.sodankyla01.R0, 2022.

Kuze, A., Suto, H., Nakajima, M., and Hamazaki, T.: Thermal and near infrared sensor for carbon observation Fourier-transform spectrometer on the Greenhouse Gases Observing Satellite for greenhouse gases monitoring, Appl. Opt., 48, 6716–6733, https://doi.org/10.1364/ao.48.006716, 2009.

Lamouroux, J., Tran, H., Laraia, A. L., Gamache, R. R., Rothman, L. S., Gordon, I. E., and Hartmann, J.-M.: Updated database plus software for line-mixing in CO_2 infrared spectra and their test using laboratory spectra in the 1.5–2.3 µm region, J. Quant. Spectrosc. Radiat. Transf., 111, 2321–2331, https://doi.org/10.1016/j.jqsrt.2010.03.006, 2010.

Lan, X., Dlugokencky, E. J., Mund, J. W., Crotwell, A. M., Crotwell, M. J., Moglia, E., Madronich, M., Neff, D., and Thoning, K. W.: Atmospheric Carbon Dioxide Dry Air Mole Fractions from the NOAA GML Carbon Cycle Cooperative Global Air Sampling Network, 1968–2021, Version: 2022-07-28 [online] https://doi.org/10.15138/wkgj-f215, 2022.

Liu, C., Wang, W., and Sun, Y.: TCCON data from Hefei(PRC), Release GGG2014.R0, https://doi.org/10.14291/tccon.ggg2014.hefei01.R0, 2018.

Machida, T., Matsueda, H., Sawa, Y., Nakagawa, Y., Hirotani, K., Kondo, N., Goto, K., Nakazawa, T., Ishikawa, K., and Ogawa, T.: Worldwide Measurements of Atmospheric CO_2 and Other Trace Gas Species Using Commercial Airlines, J. Atmos. Ocean. Technol., 25, 1744–1754, https://doi.org/10.1175/2008JTECHA1082.1, 2008.

Maksyutov, S., Takagi, H., Valsala, V. K., Saito, M., Oda, T., Saeki, T., Belikov, D. A., Saito, R., Ito, A., Yoshida, Y., Morino, I., Uchino, O., Andres, R. J., and Yokota, T.: Regional CO_2 flux estimates for 2009–2010 based on GOSAT and ground-based CO_2 observations, Atmos. Chem. Phys., 13, 9351–9373, https://doi.org/10.5194/acp-13-9351-2013, 2013.

Mendonca, J., Strong, K., Sung, K., Devi, V. M., Toon, G. C., Wunch, D., and Franklin, J. E.: Using high-resolution laboratory and ground-based solar spectra to assess CH_4 absorption coefficient calculations, J. Quant. Spectrosc. Radiat. Transf., 190, 48–59, https://doi.org/10.1016/j.jqsrt.2016.12.013, 2017.

Mlawer, E. J., Payne, V. H., Moncet, J.-L., Delamere, J. S., Alvarado, M. J., and Tobin, D. C.: Development and recent evaluation of the MT_CKD model of continuum absorption, Philos. Trans. R. Soc. A Math. Phys. Eng. Sci., 370, 2520–2556, https://doi.org/10.1098/rsta.2011.0295, 2012.

Morino, I., Yokozeki, N., Matsuzaki, T., and Horikawa, M.: TCCON data from Rikubetsu (JP), Release GGG2014.R1, https://doi.org/10.14291/tccon.ggg2014, 2016.

Morino, I., Velazco, V. A., Akihiro, H., Osamu, U., and Griffith, D. W. T.: TCCON data from Burgos, Ilocos Norte (PH), Release GGG2014.R0, https://doi.org/10.14291/tccon.ggg2020.burgos01.R0, 2018a.

Morino, I., Matsuzaki, T., and Horikawa, M.: TCCON data from Tsukuba (JP), 125HR, Release GGG2014.R2, https://doi.org/10.14291/tccon.ggg2014.tsukuba02.r2, 2018b.

Morino, I., Ohyama, H., Hori, A., and Ikegami, H.: TCCON data from Burgos, Ilocos Norte (PH), Release GGG2020.R0, https://doi.org/10.14291/tccon.ggg2020.burgos02.R0, 2022a.

Morino, I., Ohyama, H., Hori, A., and Ikegami, H.: TCCON data from Rikubetsu (JP), Release GGG2020.R0, https://doi.org/10.14291/tccon.ggg2020.rikubetsu01.R0, 2022b.

Morino, I., Ohyama, H., Hori, A., and Ikegami, H.: TCCON data from Tsukuba (JP), 125HR, Release GGG2020.R0, https://doi.org/10.14291/tccon.ggg2020.tsukuba02.R0, 2022c.

NIES GOSAT project: Release Note of Bias-corrected FTS SWIR Level 2 CO_2, CH_4 Products (V02.95/V02.96) for General Users, https://data2.gosat.nies.go.jp/doc/documents/ReleaseNote_FTSSWIRL2_BiasCorr_V02.95-V02.96_en.pdf (last access: 13 March 2023), 2020.

NIES GOSAT project: Release Note of Bias-corrected FTS SWIR Level 2 CO_2 Product (V02.97/V02.98) for General Users, https://data2.gosat.nies.go.jp/doc/documents/ReleaseNote_FTSSWIRL2_BiasCorrCO2_V02.97-V02.98_en.pdf (last access: 13 March 2023), 2021.

Noël, S., Reuter, M., Buchwitz, M., Borchardt, J., Hilker, M., Bovensmann, H., Burrows, J. P., Di Noia, A., Suto, H., Yoshida, Y., Buschmann, M., Deutscher, N. M., Feist, D. G., Griffith, D. W. T., Hase, F., Kivi, R., Morino, I., Notholt, J., Ohyama, H., Petri, C., Podolske, J. R., Pollard, D. F., Sha, M. K., Shiomi, K., Sussmann, R., Té, Y., Velazco, V. A., and Warneke, T.: XCO_2 retrieval for GOSAT and GOSAT-2 based on the FOCAL algorithm, Atmos. Meas. Tech., 14, 3837–3869, https://doi.org/10.5194/amt-14-3837-2021, 2021.

Nomura, S., Mukai, H., Terao, Y., Machida, T., and Nojiri, Y.: Six years of atmospheric CO_2 observations at Mt. Fuji recorded with a battery-powered measurement system, Atmos. Meas. Tech., 10, 667–680, https://doi.org/10.5194/amt-10-667-2017, 2017.

Nomura, S., Naja, M., Ahmed, M. K., Mukai, H., Terao, Y., Machida, T., Sasakawa, M., and Patra, P. K.: Measurement report: Regional characteristics of seasonal and long-term variations in greenhouse gases at Nainital, India, and Comilla, Bangladesh, Atmos. Chem. Phys., 21, 16427–16452, https://doi.org/10.5194/acp-21-16427-2021, 2021.

Notholt, J., Petri, C., Warneke, T., Deutscher, N. M., Buschmann, M., Weinzierl, C., Macatangay, R., and Grupe, P.: TCCON data from Bremen (DE), Release GGG2014R0, https://doi.org/10.14291/tccon.ggg2014.bremen01.R0/1149275, 2014.

Notholt, J., Petri, C., Warneke, T., Deutscher, N. M., Palm, M., and Buschmann, M.: TCCON data from Bremen (DE), Release GGG2020.R0, https://doi.org/10.14291/tccon.ggg2020.bremen01.R0, 2022.

O'Dell, C. W., Connor, B., Bösch, H., O'Brien, D., Frankenberg, C., Castano, R., Christi, M., Eldering, D., Fisher, B., Gunson, M., McDuffie, J., Miller, C. E., Natraj, V., Oyafuso, F., Polonsky, I., Smyth, M., Taylor, T., Toon, G. C., Wennberg, P. O., and Wunch, D.: The ACOS CO_2 retrieval algorithm – Part 1: Description and validation against synthetic observations, Atmos. Meas. Tech., 5, 99–121, https://doi.org/10.5194/amt-5-99-2012, 2012.

Ohyama, H., Kawakami, S., Shiomi, K., and Miyagawa, K.: Retrievals of total and tropospheric ozone from GOSAT thermal infrared spectral radiances, IEEE Trans. Geosci. Remote Sens., 50, 1770–1784, 2012.

Oshchepkov, S., Bril, A., Maksyutov, S., and Yokota, T.: Detection of optical path in spectroscopic space-based observations of greenhouse gases: Application to GOSAT data processing, J. Geophys. Res.-Atmos., 116, D14304, https://doi.org/10.1029/2010JD015352, 2011.

Parker, R., Boesch, H., Cogan, A., Fraser, A., Feng, L., Palmer, P. I., Messerschmidt, J., Deutscher, N., Griffith, D. W. T., Notholt, J.,

Wennberg, P. O., and Wunch, D.: Methane observations from the Greenhouse Gases Observing SATellite: Comparison to ground-based TCCON data and model calculations, Geophys. Res. Lett., 38, L15807, https://doi.org/10.1029/2011GL047871, 2011.

Petri, C., Vrekoussis, M., Rousogenous, C., Warneke, T., Sciare, J., and Notholt, J.: TCCON data from Nicosia (CY), Release GGG2020.R0, https://doi.org/10.14291/tccon.ggg2020.nicosia01.R0, 2022.

Pollard, D. F., Robinson, J., and Shiona, H.: TCCON data from Lauder (NZ), Release GGG2014.R0, https://doi.org/10.14291/TCCON.GGG2014.LAUDER03.R0, 2019.

Pollard, D. F., Robinson, J., and Shiona, H.: TCCON data from Lauder (NZ), 125HR, Release GGG2020.R0, https://doi.org/10.14291/tccon.ggg2020.lauder03.R0, 2022.

Rodgers, C. D.: Inverse methods for atmospheric sounding: theory and practice, World scientific, Singapore, 2000.

Rothman, L. S., Gordon, I. E., Barbe, A., Benner, D. C., Bernath, P. F., Birk, M., Boudon, V., Brown, L. R., Campargue, A., Champion, J.-P., Chance, K., Coudert, L. H., Dana, V., Devi, V. M., Fally, S., Flaud, J.-M., Gamache, R. R., Goldman, A., Jacquemart, D., Kleiner, I., Lacome, N., Lafferty, W. J., Mandin, J.-Y., Massie, S. T., Mikhailenko, S. N., Miller, C. E., Moazzen-Ahmadi, N., Naumenko, O. V, Nikitin, A. V, Orphal, J., Perevalov, V. I., Perrin, A., Predoi-Cross, A., Rinsland, C. P., Rotger, M., Šimečková, M., Smith, M. A. H., Sung, K., Tashkun, S. A., Tennyson, J., Toth, R. A., Vandaele, A. C., and Vander Auwera, J.: The HITRAN 2008 molecular spectroscopic database, J. Quant. Spectrosc. Radiat. Transf., 110, 533–572, https://doi.org/10.1016/j.jqsrt.2009.02.013, 2009.

Saeki, T., Saito, R., Belikov, D., and Maksyutov, S.: Global high-resolution simulations of CO_2 and CH_4 using a NIES transport model to produce a priori concentrations for use in satellite data retrievals, Geosci. Model Dev., 6, 81–100, https://doi.org/10.5194/gmd-6-81-2013, 2013.

Saitoh, N., Imasu, R., Ota, Y. and Niwa, Y.: CO_2 retrieval algorithm for the thermal infrared spectra of the Greenhouse Gases Observing Satellite: Potential of retrieving CO_2 vertical profile from high-resolution FTS sensor, J. Geophys. Res., 114, D17305, https://doi.org/10.1029/2008jd011500, 2009.

Saitoh, N., Kimoto, S., Sugimura, R., Imasu, R., Kawakami, S., Shiomi, K., Kuze, A., Machida, T., Sawa, Y., and Matsueda, H.: Algorithm update of the GOSAT/TANSO-FTS thermal infrared CO_2 product (version 1) and validation of the UTLS CO2 data using CONTRAIL measurements, Atmos. Meas. Tech., 9, 2119–2134, https://doi.org/10.5194/amt-9-2119-2016, 2016.

Sherlock, V., Connor, B. J., Robinson, J., Shiona, H., Smale, D., and Pollard, D.: TCCON data from Lauder (NZ), 120HR, Release GGG2014R0, https://doi.org/10.14291/tccon.ggg2014.lauder01.R0/1149293, 2014a.

Sherlock, V., Connor, B. J., Robinson, J., Shiona, H., Smale, D., and Pollard, D.: TCCON data from Lauder (NZ), 125HR, Release GGG2014R0, https://doi.org/10.14291/tccon.ggg2014.lauder02.R0/1149298, 2014b.

Sherlock, V., Connor, B., Robinson, J., Shiona, H., Smale, D., and Pollard, D. F.: TCCON data from Lauder (NZ), 120HR, Release GGG2020.R0, https://doi.org/10.14291/tccon.ggg2020.lauder01.R0, 2022a.

Sherlock, V., Connor, B., Robinson, J., Shiona, H., Smale, D., and Pollard, D. F.: TCCON data from Lauder (NZ), 125HR, Release GGG2020.R0, https://doi.org/10.14291/tccon.ggg2020.lauder02.R0, 2022b.

Shiomi, K., Kawakami, S., Ohyama, H., Arai, K., Okumura, H., Ikegami, H., and Usami, M.: TCCON data from Saga (JP), Release GGG2020.R0, https://doi.org/10.14291/tccon.ggg2020.saga01.R0, 2022.

Someya, Y. and Yoshida, Y.: Evaluating radiometric responsivity degradations of TANSO-FTS/GOSAT using principal component analysis, J. Atmos. Ocean. Technol., 37, 1877–1890, https://doi.org/10.1175/JTECH-D-19-0224.1, 2020.

Someya, Y., Imasu, R., Saitoh, N., Ota, Y., and Shiomi, K.: A development of cloud top height retrieval using thermal infrared spectra observed with GOSAT and comparison with CALIPSO data, Atmos. Meas. Tech., 9, 1981–1992, https://doi.org/10.5194/amt-9-1981-2016, 2016.

Someya, Y., Imasu, R., Shiomi, K., and Saitoh, N.: Atmospheric ammonia retrieval from the TANSO-FTS/GOSAT thermal infrared sounder, Atmos. Meas. Tech., 13, 309–321, https://doi.org/10.5194/amt-13-309-2020, 2020.

Strong, K., Mendonca, J., Weaver, D., Fogal, P., Drummond, J. R., Batchelor, R., and Lindenmaier, R.: TCCON data from Eureka (CA), Release GGG2014R1, https://doi.org/10.14291/tccon.ggg2014.eureka01.R1/1325515, 2017.

Sussmann, R. and Rettinger, M.: TCCON data from Garmisch (DE), Release GGG2014.R0, https://doi.org/10.14291/tccon.ggg2014, 2015.

Sussmann, R. and Rettinger, M.: TCCON data from Zugspitze (DE), Release GGG2014R1, https://doi.org/10.14291/tccon.ggg2014.zugspitze01.R1, 2018.

Takemura, T., Okamoto, H., Maruyama, Y., Numaguti, A., Higurashi, A., and Nakajima, T.: Global three-dimensional simulation of aerosol optical thickness distribution of various origins, J. Geophys. Res., 105, 17853–17873, https://doi.org/10.1029/2000jd900265, 2000.

Taylor, T. E., O'Dell, C. W., Crisp, D., Kuze, A., Lindqvist, H., Wennberg, P. O., Chatterjee, A., Gunson, M., Eldering, A., Fisher, B., Kiel, M., Nelson, R. R., Merrelli, A., Osterman, G., Chevallier, F., Palmer, P. I., Feng, L., Deutscher, N. M., Dubey, M. K., Feist, D. G., García, O. E., Griffith, D. W. T., Hase, F., Iraci, L. T., Kivi, R., Liu, C., De Mazière, M., Morino, I., Notholt, J., Oh, Y.-S., Ohyama, H., Pollard, D. F., Rettinger, M., Schneider, M., Roehl, C. M., Sha, M. K., Shiomi, K., Strong, K., Sussmann, R., Té, Y., Velazco, V. A., Vrekoussis, M., Warneke, T., and Wunch, D.: An 11-year record of XCO_2 estimates derived from GOSAT measurements using the NASA ACOS version 9 retrieval algorithm, Earth Syst. Sci. Data, 14, 325–360, https://doi.org/10.5194/essd-14-325-2022, 2022.

TCCON: Total Carbon Column Observing Network (TCCON), TCCON [data set], https://tccondata.org, last access: 13 March 2023.

Té, Y., Jeseck, P., and Janssen, C.: TCCON data from Paris (FR), Release GGG2014.R0, https://doi.org/10.14291/TCCON.GGG2014.PARIS01.R0/1149279, 2014.

Té, Y., Jeseck, P. and Janssen, C.: TCCON data from Paris (FR), Release GGG2020.R0, https://doi.org/10.14291/tccon.ggg2020.paris01.R0, 2022.

Tohjima, Y., Mukai, H., Machida, T., Nojiri, Y., and Gloor, M.: First measurements of the latitudinal atmospheric O2 and CO_2 distributions across the western Pacific, Geophys. Res. Lett., 32, L17805, https://doi.org/10.1029/2005GL023311, 2005.

Toon, G. C.: Atmospheric Line List for the 2014 TCCON Data Release, https://doi.org/10.14291/TCCON.GGG2014.ATM.R0/1221656, 2015a.

Toon, G. C.: Solar Line List for the TCCON 2014 Data Release, https://doi.org/10.14291/TCCON.GGG2014.SOLAR.R0/1221658, 2015b.

Tran, H. and Hartmann, J.-M.: An improved O_2 A band absorption model and its consequences for retrievals of photon paths and surface pressures, J. Geophys. Res.-Atmos., 113, D18104, https://doi.org/10.1029/2008JD010011, 2008.

Tran, H., Boulet, C., and Hartmann, J.-M.: Line mixing and collision-induced absorption by oxygen in the A band: Laboratory measurements, model, and tools for atmospheric spectra computations, J. Geophys. Res.-Atmos., 111, D15210, https://doi.org/10.1029/2005JD006869, 2006.

Warneke, T., Messerschmidt, J., Notholt, J., Weinzierl, C., Deutscher, N. M., Petri, C., Grupe, P., Vuillemin, C., Truong, F., Schmidt, M., Ramonet, M., and Parmentier, E.: TCCON data from Orléans (FR), Release GGG2014R0, https://doi.org/10.14291/tccon.ggg2014.orleans01.R0/1149276, 2014.

Warneke, T., Petri, C., Notholt, J., and Buschmann, M.: TCCON data from Orléans (FR), Release GGG2020.R0, https://doi.org/10.14291/tccon.ggg2020.orleans01.R0, 2022.

Wennberg, P. O., Wunch, D., Roehl, C. M., Blavier, J.-F., Toon, G. C., and Allen, N. T.: TCCON data from Caltech (US), Release GGG2014.R1, https://doi.org/10.14291/tccon.ggg2014.pasadena01.r1/1182415, 2015.

Wennberg, P. O., Roehl, C., Blavier, J.-F., Wunch, D., Landeros, J., and Allen, N.: TCCON data from Jet Propulsion Laboratory (US), 2011, Release GGG2014R1, https://doi.org/10.14291/tccon.ggg2014.jpl02.R1/1330096, 2016a.

Wennberg, P. O., Wunch, D., Roehl, C., Blavier, J.-F., Toon, G. C., Allen, N., Dowell, P., Teske, K., Martin, C., and Martin., J.: TCCON data from Lamont (US), Release GGG2014R1, https://doi.org/10.14291/tccon.ggg2014.lamont01.R1/1255070, 2016b.

Wennberg, P. O., Roehl, C. M., Wunch, D., Toon, G. C., Blavier, J.-F., Washenfelder, R., Keppel-Aleks, G., Allen, N. T., and Ayers, J.: TCCON data from Park Falls (US), Release GGG2014.R1, https://doi.org/10.14291/TCCON.GGG2014.PARKFALLS01.R1, 2017.

Wennberg, P. O., Roehl, C. M., Wunch, D., Blavier, J.-F., Toon, G. C., Allen, N. T., and Laughner, J.: TCCON data from Caltech (US), Release GGG2020.R0, https://doi.org/10.14291/tccon.ggg2020.pasadena01.R0, 2022a.

Wennberg, P. O., Roehl, C. M., Blavier, J.-F., Wunch, D., and Allen, N. T.: TCCON data from Jet Propulsion Laboratory (US), 2011, Release GGG2020.R0, https://doi.org/10.14291/tccon.ggg2020.jpl02.R0, 2022b.

Wennberg, P. O., Wunch, D., Roehl, C. M., Blavier, J.-F., Toon, G. C., and Allen, N. T.: TCCON data from Lamont (US), Release GGG2020.R0, https://doi.org/10.14291/tccon.ggg2020.lamont01.R0, 2022c.

Wennberg, P. O., Roehl, C. M., Wunch, D., Toon, G. C., Blavier, J.-F., Washenfelder, R., Keppel-Aleks, G., and Allen, N. T.: TCCON data from Park Falls (US), Release GGG2020.R0, https://doi.org/10.14291/tccon.ggg2020.parkfalls01.R0, 2022d.

Wunch, D., Toon, G. C., Blavier, J.-F. L., Washenfelder, R. A., Notholt, J., Connor, B. J., Griffith, D. W. T., Sherlock, V., and Wennberg, P. O.: The Total Carbon Column Observing Network, Philos. Trans. R. Soc. a-Mathematical Phys. Eng. Sci., 369, 2087–2112, https://doi.org/10.1098/rsta.2010.0240, 2011.

Wunch, D., Mendonca, J., Colebatch, O., Allen, N., Blavier, J.-F. L., Roche, S., Hedelius, J. K., Neufeld, G., Springett, S., Worthy, D. E. J., Kessler, R., and Strong, K.: TCCON data from East Trout Lake (CA), Release GGG2014R1, https://doi.org/10.14291/tccon.ggg2014.easttroutlake01.R1, 2017.

Wunch, D., Mendonca, J., Colebatch, O., Allen, N. T., Blavier, J.-F., Kunz, K., Roche, S., Hedelius, J., Neufeld, G., Springett, S., Worthy, D., Kessler, R., and Strong, K.: TCCON data from East Trout Lake, SK (CA), Release GGG2020.R0, https://doi.org/10.14291/tccon.ggg2020.easttroutlake01.R0, 2022.

Yokota, T., Yoshida, Y., Eguchi, N., Ota, Y., Tanaka, T., Watanabe, H., and Maksyutov, S.: Global Concentrations of CO_2 and CH_4 Retrieved from GOSAT: First Preliminary Results, SOLA, 5, 160–163, https://doi.org/10.2151/sola.2009-041, 2009.

Yoshida, Y., Ota, Y., Eguchi, N., Kikuchi, N., Nobuta, K., Tran, H., Morino, I., and Yokota, T.: Retrieval algorithm for CO_2 and CH_4 column abundances from short-wavelength infrared spectral observations by the Greenhouse gases observing satellite, Atmos. Meas. Tech., 4, 717–734, https://doi.org/10.5194/amt-4-717-2011, 2011.

Yoshida, Y., Kikuchi, N., and Yokota, T.: On-orbit radiometric calibration of SWIR bands of TANSO-FTS onboard GOSAT, Atmos. Meas. Tech., 5, 2515–2523, https://doi.org/10.5194/amt-5-2515-2012, 2012.

Yoshida, Y., Kikuchi, N., Morino, I., Uchino, O., Oshchepkov, S., Bril, A., Saeki, T., Schutgens, N., Toon, G. C., Wunch, D., Roehl, C. M., Wennberg, P. O., Griffith, D. W. T., Deutscher, N. M., Warneke, T., Notholt, J., Robinson, J., Sherlock, V., Connor, B., Rettinger, M., Sussmann, R., Ahonen, P., Heikkinen, P., Kyrö, E., Mendonca, J., Strong, K., Hase, F., Dohe, S., and Yokota, T.: Improvement of the retrieval algorithm for GOSAT SWIR XCO_2 and XCH_4 and their validation using TCCON data, Atmos. Meas. Tech., 6, 1533–1547, https://doi.org/10.5194/amt-6-1533-2013, 2013.

Zhou, M., Wang, P., Kumps, N., Hermans, C., and Nan, W. X.: TCCON data from Xianghe, China, Release GGG2020.R0, https://doi.org/10.14291/tccon.ggg2020.xianghe01.R0, 2022.